博士論文

$LnF_3:Eu^{3+}$（Ln＝La,Gd）ナノ粒子の母材制御と発光特性

2011 年 2 月

張 小 婷

Host Control and Photoluminescence Properties of $LnF_3:Eu^{3+}$(Ln=La, Gd) Nanoparticles

Xiaoting Zhang

January, 2011

Thesis supervisor:

Associate Professor Dr. Yukari Ishikawa

Graduate School of Engineering

Nagoya Institute of Technology

Contents

Chapter 1. Introduction

1.1 General introduction

Phosphors play important roles in our society for their wide applications in industry, in military and in everyday life. Whether one engages in laser surgery with a neodymium-YAG laser or one enjoys 3D movies without any eyewear at home, the development of these materials is scientifically of great interest.

Phosphors are formed from host-crystal and activator ingredients which are isostructural. Typical activators are rare-earth or transition-metal ions. In contrast to transition metals, rare-earth (RE) ions have the unique properties : a large number of possible energetic states of partially filled $4f^n$ electron shell ($1<n<14$)), screening effect produced by their completely filled $5s^2 5p^6$ electron shells (which weakens the influence of external electric and magnetic fields on 4f electrons) and small stabilization due to crystal-field effect. These unique properties make them very attractive activator ions in solid state lasers and phosphors covering a wide spectral range from infrared (IR) to ultraviolet (UV) and vacuum ultraviolet (VUV) spectral regions.

Lanthanide trifluorides (LnF_3) are very suitable hosts for doping RE ions because the lanthanide ions could be substituted easily with RE ions with the same valence, and more significantly, they have low phonon energy that makes it possible to reduce the nonradiative de-excitation probability of the luminescent RE ions by the multiphonon relaxation.

Recently, many studies on rare-earth ions doped LnF_3 luminescent materials have focused on the preparation of various kinds of nanoparticles in controlled shape, size, and crystal structure and thus to tailor their luminescence properties [1,2,3]. LnF_3 with different size and morphologies such as fullerene-like nanoparticles [4], bundle-like particles [5], and nano-plates [6] exhibited different optical properties. EuF_3 with hexagonal structure shows stronger luminescence intensity than that with orthorhombic structure was also reported [7]. It is well known that the optical properties of luminescent nanomaterials are enormously affected by their shapes, sizes and structures [8,9,10], but the mechanism of how particle size and crystal structure influence luminescence properties of doped rare-earth ions are still far from being well understood. In order to obtain phosphors with higher efficiencies and strong luminescence intensity it is necessary to know how the host size and structure affect activator luminescence properties. This thesis focused on investigating the roles of host structures (particle size, particle shape, polytype and activator location) playing in activator luminescence properties. These basic studies of host structure will be a guiding principle to synthesize high performance rare-earth ions doped LnF_3 materials.

Lanthanum fluoride (LaF_3) is an excellent host matrix for luminescent materials because of its low phonon energies and has been used as an extreme pressure and antiwear additive in grease and as solid lubricant under high temperature because of its fairly low hardness, high melting point, and good resistance to thermal and chemical attack [6]. RE-doped LaF_3 (nanocrystals) NCs have received much attention for their wide applications in optics and optoelectronics (e.g., lighting and displays, optical amplifiers, and lasers), microelectronics and especially biological labels and have been prepared via various chemical methods such as modified precipitation [11], polyol [12], and solvothermal method [13]. A synthesis method of size tunable $LaF_3:Eu^{3+}$ nanocrystals with cetyltrimethylammonium bromide (CTAB) as size control agent via a hydrothermal rout was developed in order to illustrate the correlation between particles size, Eu^{3+} ions located position and luminescence properties. In LnF_3 materials, the medial SmF_3, EuF_3 and GdF_3 undergoing the phase transition between hexagonal and orthorhombic, GdF_3 is also a good alternative for LaF_3. Because of a 4f energy-level overlap between the ^6P_J states of Gd^{3+} and the ^5H_J states of Eu^{3+}, energy transfer from Gd^{3+} to Eu^{3+} is possible [14]. So, polytype $GdF_3:Eu^{3+}$ nanocrystals were selected to illustrate the effect of host polytypes on luminescence properties of doped Eu^{3+} ions.

In Chapter 1, general properties of the Eu ion used as activator and the structure of LaF_3 (GdF_3) used as host in this work are discussed. Theories of Rietveld method and Förster resonance energy transfer mechanism are introduced.

In Chapter 2 a new method to analyze Eu^{3+} ions location in host particle is described. This method is based on Eu^{3+} ions typical luminescence properties. Via analyzing $^5D_0 - {}^7F_{1,2}$ decay curves in Eu^{3+} ions with double exponential function [15] by a least-square fitting method, fractions of doped Eu^{3+} ions located in different sites in host particles can be estimated. This method is used throughout this thesis.

Chapter 3 describes the development of synthesis method of size tunable $LaF_3:Eu^{3+}$ nanoparticles and the characterization of their size, crystals structure and luminescence properties. Size effects on luminescence properties of these samples were investigated. It is pointed out that the Eu^{3+} ion location depends on particle size, and how the location changes was also discussed.

Chapter 4 introduces a novel simple method to prepare polytype (hexagonal and orthorhombic) $GdF_3:Eu^{3+}$ nanoparticles crystals. The polytype structures and morphologies are characterized by XRD patterns, SEM and TEM images, their luminescence properties are discussed based on the photoluminescence (PL), photoluminescence excitation (PLE) and decay curves spectra, how the polytype structures influence luminescence properties is described.

A summery was described in Chapter 5.

In this study, by analyzing Eu^{3+} luminescence properties in size tuned $LaF_3:Eu^{3+}$ nanoparticles it was found that Eu^{3+} ions prefer to locate in a high symmetric site in LaF_3 lattice matrix as their particle size increased. It means that in large particles most of Eu^{3+} ions were situated in the environment with few defects, which engaged strong PL. Polytype studies of Eu^{3+} doped GdF_3 nanoparticles indicated that the interatomic distances between Gd^{3+} ions in the hexagonal structure were shorter than those in the orthorhombic structure. Much more efficient energy transfer is expected from Gd to Eu in the hexagonal structure than that in the orthorhombic structure as the most of Eu ions (about 70%) in both polytype $GdF_3:Eu^{3+}$ occupied Gd sites.

1.2 Eu ion luminescence properties

Being special important rare-earth ions, Eu ions energy levels of 4f orbitals are not degenerate because of electronic repulsion, spin-orbit coupling, and (in a coordination environment) the ligand field. The strongest interaction, the electronic repulsion between the electrons, disrupts the degeneracy of the 4f energy levels and yields terms with separations in the order of 10^4 cm^{-1}. Spin-orbit coupling is the interaction between the magnetic moments of the electrons due to their spin (spin angular momentum) and the magnetic moments due to their movement around the nucleus (orbital angular momentum). This causes further splitting of the energy levels into so call J-states. The splitting of these energy levels is in the order of 10^3 cm^{-1}. The J-degeneracy is partially removed in a coordination environment by the ligand field. These splittings are in the order of 10^2 cm^{-1} (see Figure 1-1).

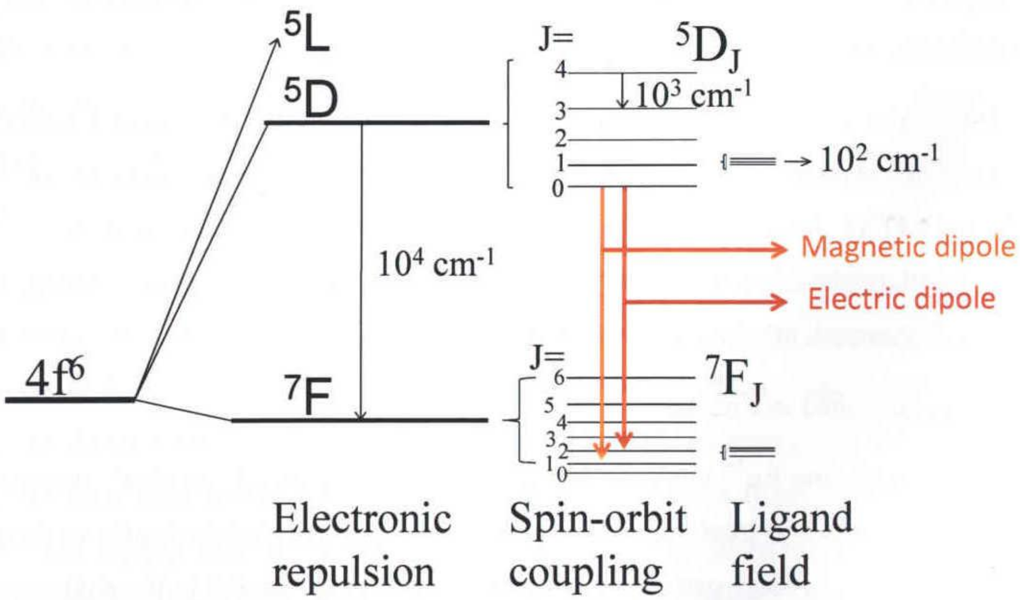

Figure 1-1 Splitting of the 4f energy levels of Eu^{3+} as a result of electronic repulsion, spin-orbit coupling, and the ligand field.

Eu^{3+} luminescence can be structures-probe apart from its application in phosphor materials. This is possible for the reason that Eu^{3+} has several structure-dependent transitions enabling one to gain insight about the site that it occupies in a given host. The optical transitions of Eu^{3+} are a special case in the theory of induced electric dipole transitions. The induced electric dipole transitions have an additional selection rule ($\Delta J = \pm 2, \pm 4, \cdots$). If the initial level has J = 0, as is the case for Eu^{3+} ($^5D_0$): transitions to odd J are forbidden. This generally results in the following emission spectrum [16] (in Figure 1-2):

$^5D_0 \rightarrow {}^7F_0$ (~580 nm): extremely weak, induced electric dipole (J = 0 to J′ = 0 is forbidden).

$^5D_0 \rightarrow {}^7F_1$ (~590 nm): magnetic dipole emission.

$^5D_0 \rightarrow {}^7F_2$ (~613 nm): hypersensitive induced electric dipole emission.

$^5D_0 \rightarrow {}^7F_3$ (~650 nm): extremely weak, induced electric dipole emission.

$^5D_0 \rightarrow {}^7F_4$ (~700 nm): weak, induced electric dipole emission.

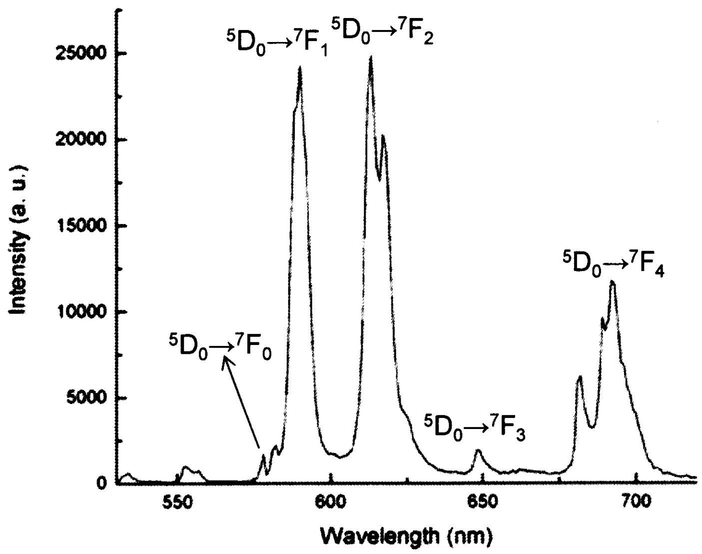

Figure 1-2 Emission spectrum from $^5D_0$ level of Eu^{3+} ion in LaF_3 particles.

The emission band centered around at 590 nm, corresponding to $^5D_0 \rightarrow ^7F_1$ transition that is magnetic dipole in character, is relatively strong and independent of the local symmetry of the Eu^{3+} ions [15]. The electric dipole $^5D_0 \rightarrow ^7F_2$ transition centered around at 613 nm is hypersensitive and extremely sensitive to the local symmetry of Eu^{3+} ions. Kirby and Richardson [17] established that the relative intensity of $^5D_0 \rightarrow ^7F_2$ and $^5D_0 \rightarrow ^7F_1$ emission is a good measure of the local environment of the Eu^{3+} ion. In a high symmetric environment, the magnetic dipole $^5D_0 \rightarrow ^7F_1$ transition of Eu^{3+} is dominating, whereas distortion of the symmetry around the ion causes an intensity enhancement of electric dipole transitions such as the hypersensitive $^5D_0 \rightarrow ^7F_2$ transition. It is clear that the $I_{(5D0 \rightarrow 7F2)}/I_{(5D0 \rightarrow 7F1)}$ intensity ratio, called the asymmetry ratio, A,[18,19] give a measure of the local environment of the Eu^{3+} ion. For this special characteristic, Eu^{3+} ion was chosen as a doping rare-earth to investigate how the hosts particle size and polytype structure influence the luminescence properties of doped ions in our work,.

1.3 LaF_3 and GdF_3 crystal structure

1.3.1 LaF_3 crystal structure

LaF_3 nanocrystal has received particular attention because of its good qualities: adequate thermal and environmental stability, low phonon energy (as low as 350 cm^{-1}), ability of being easily doped with rare-earth ions. All of these good qualities made LaF_3 nanocrystas become one of the most efficient host materials for luminescence materials [20,21,22]. Therefore, the study of LaF_3 nano-crystals has attracted considerable interest. Single-crystal studies by Mansmann (1965) [23], Zalkin, Templeton and Hopkins (1966) [24] and A. K. Cheetham and AND B. E. F. Fender (1975) [25] indicate the space group $P\bar{3}c1$, the result was supported by Raman measurements (Bauman and Porto, 1967 [26]). On the other hand the X-ray and neutron measurements of de Rango, Tsoucaris and Zelwer (1966) [27] have been interpreted in $P6_3cm$, while Afanasiev, Habuda and Lundin speculated $P6_3/mcm$ on the basis of other results on CeF_3, PrF_3 and NdF_3 (1972) [28]. Recently, more and more study results (I. Brach, and H. Schulz, 1985 [29], B. Winkler, K. Knorr, and V. Milman, 2003 [30], T.J. Udovic, Q.Z. Huang, A. Santoro and J.J. Rush 2008 [31])prefer to $P\bar{3}c1$ space group. In Table 1-1 list the structure parameters of LaF_3 reported by Udovic group.

Table 1-1 Atomic parameters of LaF_3 in $P\bar{3}c1$ space group

LaF_3	Cell dimensions: a= b=7.1907Å, c=7.3531Å		
	X	Y	Z
La	0.6596	0	0.25
F(1)	0.3655	0.0537	0.0813
F(2)	0	0	0.25
F(3)	0.3333	0.6667	0.1873

Figure 1-3 shows a LaF_3 crystal structure with hexagonal lattice with $P\bar{3}c1$ space group. La^{3+} ions in LaF_3 are situated at a site of C_2 symmetry, each La^{3+} ion being surrounded by 11 F^{-1} ions, the coordination polyhedron is a distortion of a tricapped trigonal prism with two extra ligands on the 3-fold axis. There are six sites with identical electric environment oriented in three directions separated by angles of 60°. The z-axes of the C_2 sites are perpendicular to the z-axis of the crystal and the x-axis of each site is parallel to the z-axis of the crystal.

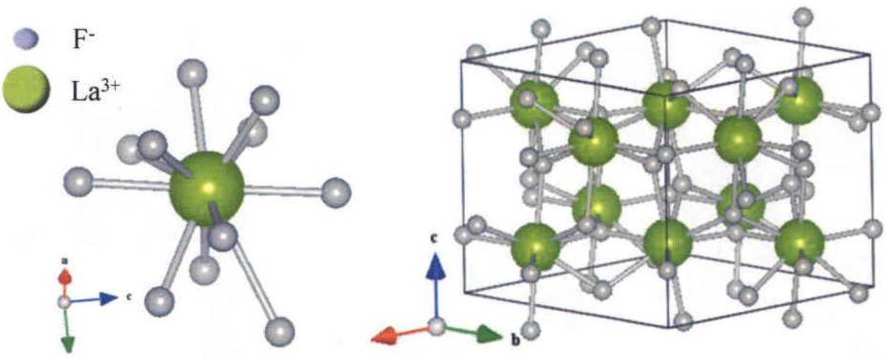

Figure 1-3 Unit-cell structure of hexagonal LaF_3 crystal (hexagonal).

In LaF_3 hexagonal structure, there is no asymmetric center in it, so the electric dipole $^5D_0 \rightarrow {}^7F_2$ transition of Eu^{3+} ion doped in LaF_3 matrix is not complete forbidden. The analysis of $^5D_0 \rightarrow {}^7F_1$ and $^5D_0 \rightarrow {}^7F_2$ luminescence decay curves can be used in the method of Eu^{3+} ions located position estimation in host particle, which is mentioned in Chapter 3.

1.3.2 GdF_3 crystal structure

For rare-earth ions, ionic radium decreased as atomic number increased from La to Lu. It is reported by Mansmann [32] that in lanthanide trifluorides (LnF_3) crystals when the ionic radius of the lanthanide earth r_{LN} decreases, the fluorine ions tend to touch each other, resulting in a repulsive energy which induced the LnF_3 structure change from hexagonal to orthorhombic. Zalkin et al.[24] established the current accepted structure of the LaF_3. Which was described as trigonal with space group $P\bar{3}c1$ and Z = 6 as mentioned in Section 1.3.1. The light rare earths fluorides from La to Nd crystallize in this structure. All other rare earth fluorides crystallize at room temperature in the orthorhombic structure determined by Zalkin and Templeton [33] for LnF_3, also referred as β-YF_3, space group Pnma and Z = 4. The orthorhombic structure of YF_3 was showed in Figure 1-4. The unit cell is a distorted hexagonal LaF_3 lattice, the basic unit of the orthorhombic structure YF_3 is a tricapped prism with nine fluorine ions surrounding the Y^{3+} ion, six fluorine ions are at the corners of the irregular trigonal prism with a Y ion at the center and the three other fluorine ions are in front of the three side faces of this trigonal prism.

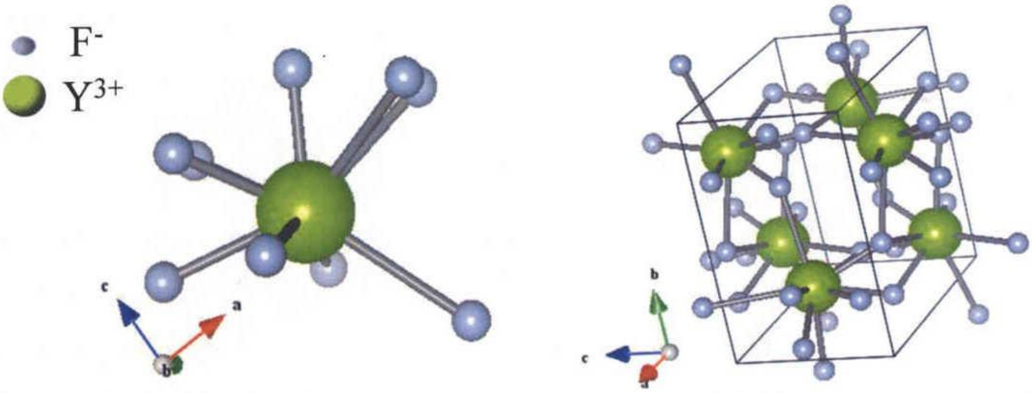

Figure 1-4 Unit-cell structure of orthorhombic YF_3 crystal (orthorhombic).

The intermediate SmF_3, EuF_3 and GdF_3 have the polytype structures of hexagonal and orthorhombic. Recently, stronger luminescence from Eu^{3+} in hexagonal EuF_3 than that in orthorhombic one is reported [34]. This fact suggests that polytype control of matrix LnF_3 enables to increase light emitting probability of doped rare earth in LnF_3 by changing atomic coordination around the doped rare-earth.

GdF_3 luminescence material is a well-known wide band-gap material that has excellent luminescent properties in visible and vacuum ultraviolet regions. In this thesis GdF_3 was selected as the host to detect the correlation between the luminescence properties and crystals structures.

1.4 Förster Resonance Energy Transfer

Sensitization via energy transfer provides a means to deliver energy to a donor that inefficiently couples to the excitation source. The acceptor at first absorbs the excitation energy and then transfers it to the donor through a nonradiative process. This nonradiative energy transfer is generally called by the Förster resonance energy transfer whose practical description was first given by Förster in 1946 [35].

According to Förster resonance energy transfer theory, the energy transfer arises from a dipole-dipole interaction between the electronic states of the donor and the acceptor, and does not involve the emission and re-absorption of a light field. Resonant transfer occurs when the oscillations of an optically induced electronic energy on the donor are coherent with the electronic energy gap of the acceptor. The strength of the interaction depends on the magnitude of a transition dipole interaction, which depends on the magnitude of the donor and acceptor transition matrix elements, and the alignment and separation of the dipoles. The probability of energy transfer, P_{AB}, depends on the square of the energy overlap and inversely on sixth power of the distance between the donor and acceptor, expressed as below [36] :

$$P_{AB} = 1.4 \times 10^{24} f_A f_B S / [\Delta E^2 R^6] \qquad \text{Eq.(1-1)}$$

f_A,f_B: Oscillator strengths of the donor and acceptor, respectively

S: Overlap of donor emission and acceptor absorption;

ΔE: Transition energy;

R: Distance between the donor and acceptor.

Förster resonance energy transfer theory is used in chemical science, particularly in scintillators and chemical sensors. In polymer science, it is used to examine the interpenetration of polymer chains, phase separation, compatibility between polymers, interdiffusion of latex particles, interface thickness in blends of polymers, and light-harvesting polymers, among others [37]. In this thesis, it is used to discuss how the polytype structures influence the Eu^{3+} luminescence properties.

1.5 Rietveld refinement method

Rietveld refinement method is used for the characterization of crystalline materials from powder diffraction data and invented by Hugo M. Rietveld [38]. Rietveld method is now widely recognized to be uniquely valuable for structural analyses of nearly all classes of crystalline materials from X-ray and neutron powder diffraction data.

Be a complete powder-diffraction-pattern fitting technique, the goal of the Rietveld method is to minimize the residual function using a non-linear least squares method:

$$WSS = \sum_i w_i (I_i^{exp} - I_i^{calc})^2, \quad w_i = \frac{1}{\sqrt{I_i^{exp}}} \qquad \text{Eq.(1-2)}$$

The intensity of diffraction spectrum is calculated by the classical intensity equation:

$$I_i^{calc} = S_F \sum_{j=1}^{Nphase} \frac{f_j}{V_j^2} \sum_{k=1}^{Npeaks} L_k \left|F_{k,j}\right|^2 S_j \left(2\theta_i - 2\theta_{k,j}\right) P_{k,j} A_j + bkg_i \qquad \text{Eq.(1-3)}$$

The spectrum (at a 2θ point i) is determined by background value (bkg_i), diffraction intensity ($S_F \sum_{j=1}^{Nphase} \frac{f_j}{V_j^2} \sum_{k=1}^{Npeaks} L_k \left|F_{k,j}\right|^2$) which depend on the crystal structure, quantity, cell volume, texture, stress, chemistry etc and determines the height of the peaks and line broadening ($S_j(2\theta_i - 2\theta_{k,j})$) which determined the shape of the peaks. Every parameter written in term can be refined; from the refinement results microstructure parameters can be obtained.

In Rietveld refinement process will adjust the finable parameters until the residual (Eq.(1-2)) is minimized in some senses, that is, a "best fit" of the entire calculated pattern to the entire observed pattern will be obtained. There are several criteria R-factors now commonly used [39], where I_k is the intensity assigned to the k_{th} Bragg reflection at the end of the refinement cycles, y_i is the intensity at the ith step.

$$R_F = \frac{\sum\left|\left((I_k(obs))^{1/2} - (I_k(calc))^{1/2}\right)\right|}{\sum (I_k(obs))^{1/2}} \qquad \text{(R- structure factor)} \qquad \text{Eq.(1-4)}$$

$$R_B = \frac{\sum |I_K(obs) - I_K(calc)|}{\sum I_K(obs)} \qquad \text{(R-bragg factor)} \qquad \text{Eq.(1-5)}$$

$$R_P = \frac{\sum |Y_i(obs) - Y_i(calc)|}{\sum Y_i(obs)} \qquad \text{(R-pattern)} \qquad \text{Eq.(1-6)}$$

$$R_{wp} = \left\{\frac{\sum W_i(Y_i(obs)-Y_i(calc)^2)}{\sum W_i(Y_i(obs))^2}\right\}^{1/2} \quad \text{(R-weighted pattern)} \qquad \text{Eq.(1-7)}$$

$$R_{exp} = \left(\frac{(N-P)}{\sum_{i=1}^{N}[W_i I_i^{exp}]^2}\right)^{1/2} \quad \text{(R-expected factor)} \qquad \text{Eq.(1-8)}$$

$$S = \frac{R_{wp}}{R_{exp}} \quad \text{(good fitness factor)} \qquad \text{Eq.(1-9)}$$

Among these factors, R_{wp} is the most meaningful, because R_{wp} factor cannot be biased in favor of the model being used, since it best reflects the progress of the refinement. Above the R-factors, the "goodness of fit" factor S is another useful numerical criterion, a value about 1.3 is usually considered to be quite satisfactory and a value smaller than 1.5 indicate that the fitted model accounts for the data well.

In this thesis, the software program RIETAN-FP (Izumi and Ikeda, 2000) [40] was used to refine the size-tunable LaF_3 and polytype GdF_3 structure.

1.6 References

1. A.P. Alivisatos, “Semiconductor clusters, nanocrystals, and quantum dots” Science **1996**, 271, 933-937.

2. J.T. Hu, T.W. Odom, C.M. Lieber, “Chemistry and physics in one dimension: synthesis and properties of nanowires and nanotubes” Acc. Chem. Res. **1999**, 32, 435-445.

3. Y.W. Jun, J.S. Choi, J.A. Cheon, “Shape control of semiconductor and metal oxide nanocrystals through nonhydrolytic colloidal routes” Chem., Int. Ed. **2006**, 45, 3414-3439.

4. X. Wang, Y.D. Li, “Rare earth compounds nanowires, nanotubes and fullerene-like nanoparticles: synthesis, characterization and properties” Chem. Eur. J. **2003**, 9, 5627-5635.

5. X. Wang, Y.D. Li, “Fullerene-like rare-earth nanoparticles” Chem. Int. Ed. **2003**, 42, 3497-3500.

6. Y. Cheng, Y.S. Wang, Y.H. Zheng, Y.J. Qin, “Two-step self-assembly of nanodisks into plate-built cylinders through oriented aggregation”, Phys. Chem. B **2005**, 109, 11548-11551.

7. M. Wang, Q.L. Huang, J.M. Hong, X.T. Chen, Z.L. Xue, “Selective synthesis and characterization of nanocrystalline EuF_3 with orthorhombic and hexagonal structures” Cryst. Grow. Des. **2006** 6, 1972-1874.

8. J. Hu, L. Li, W. Yang, L. Manna, L. Wang, A. P. Alivisatos, “Linearly polarized emission from colloidal semiconductor quantum rods”, Science **2001**, 292, 2060-2063.

9. A. L. Pan, H. Yang, R. Yu, B. S. Zou, “Color-tunable photoluminescence of alloyed CdSxSe1-x nanobelts” Nanotechnology **2006**, 17, 1083-1086.

10. L. S. Li, J. T. Hu, W. D. Yang, A. P. Alivisatos, "Band gap variation of size- and shape-controlled colloidal CdSe quantum rods", Nano Lett. **2001**, 1, 349-351.

11. (a) J. F. Zhou, Z. S. Wu, Z. J. Zhang, W. M. Liu, H. X. Dang, "Study on an anti-wear and extreme pressure additive of surface coated LaF_3 nanoparticles in liquid paraffin" Wear **2001**, 249, 333–337.

(b) J.W. Stouwdam, F.C.J.M. van Veggel, "Near-infrared emission of redispersible Er^{3+}, Nd^{3+}, and Ho^{3+} doped LaF_3 nanoparticles," Nano Lett. **2002**, 2, 733–737.

(c) G.S. Yi, G.M. Chow, "Colloidal LaF_3: Yb,Er, LaF_3:Yb,Ho and LaF_3:Yb,Tm nanocrystals with multicolor upconversion fluorescence," J. Mater. Chem. **2005**, 15, 4460–4464.

12. (a) Y. Wei, F.Q. Lu, X.R. Zhang, D.P. Chen, "Polyol-mediated synthesis of water-soluble LaF_3:Yb, Er upconversion fluorescent nanocrystals" Mater. Lett. **2007**, 61, 1337–1340.

(b) Y. Wang, W.P. Qin, J.S. Zhang, C.Y. Cao, J.S. Zhang, Y. Jin, P.F. Zhu, G.D. Wei, G.F. Wang, L.L. Wang, "Synthesis and green upconversion fluorescence of colloidal $La_{0.78}Yb_{0.20}Er_{0.02}$ F_3/ SiO_2 core/shell nanocrystals" J. Solid State Chem. **2007**, 180, 2268–2272.

13. (a) L.Y. Wang, Y.D. Li, "Luminescent nanocrystals for nonenzymatic glucose concentration determination", J. Chem. Eur. **2007**, 13, 4203–4207.

(b) C.X. Li, X. M. Liu, P. P. Yang, C. M. Zhang, H. Z. Lian, J. Lin, "LaF_3, CeF_3, CeF_3:Tb^{3+}, and CeF_3:Tb^{3+}@LaF_3 (core-shell) nanoplates: hydrothermal synthesis and luminescence properties" J. Phys. Chem. C **2008**, 112, 2904–2910.

(c) G.J.H. De, W.P. Qin, J.S. Zhang, D. Zhao, J.S. Zhang, "Bright-green upconversion emission of hexagonal LaF_3 : Yb^{3+},Er^{3+} nanocrystals" Chem. Lett. **2005**, 34, 914–915.

14. S. Fujihara, S. Koji, T. Kimura, “Structure and optical properties of (Gd,Eu)F_3-nanocrystallized sol-gel silica films”. J. Mater. Chem., **2004**, 14: 1331-1335.

15. R.D. Peacock, “The intensities of lanthanide f-f transltlons” in “Structure and Bonding”, **1975**, 22, 83-122.

16. E. Bovero, F.C.J.M. Van Veggel, “Conformational characterisation of Eu^{3+}-doped LaF_3 core-shell nanoparticles through luminescence anisotropy studies”, J. Phys. Chem. C, **2007**, 111, 4529-4534.

17. Andrew. F. Kirby and F.S. Richardson, “Detailed analysis of the optical absorption and emission spectra of europium(3+) in the trigonal (C_3) $Eu(DBM)_3.H_2O$ system”, J. Phys. Chem. **1983**, 87, 2544-2556.

18. J.H. Kim and P.H. Holloway, “Room-temperature photoluminescence and electro luminescence properties of sputter-grown gallium nitride doped with europium”, J. Appl. Phys. **2004**, 95, 4787-4790.

19. L. Chen, Y. Liu and Y. Li, “Preparation and characterization of $ZrO_2:Eu^{3+}$ phosphors”, J. Alloys. Com., **2004**, 381, 266-271.

20. H.R. Zheng, X.T. Wang, D.M.J. ejneka, “ Up-converted emission in Pr^{3+} doped fluoride nanocrystals-based oxyfluoride glass ceramics”, J. Lumin. **2004**, 108, 395-399.

21. X.J. Wang, S.H. Huang, R. Reeves, W. Well, M.J. Dejneka, R.S. Meltzer, W.M. Yen, “Studies of the spectroscopic properties of Pr^{3+} doped LaF_3 nanocrystals/glass”, J. Lumin. **2001**, 94/95, 229-233.

22. S.Tanabe, H.Hayashi, T.Hanada, N.Onodera, “Fluorescence properties of Er^{3+} ions in glass ceramics containing LaF_3 nanocrystals”, Opt. Mater. **2002**, 19, 343-349.

23. M. Mansmann, “Die Kristallstruktur von Lanthantrifluorid” Z. Kristallogr. **1965**, 122, 375-398.

24. A. Zalkin, D.H. Templeton, and T.E. Hopkins, "The atomic parameters in the lanthanum trifluoride structure" Inorg. Chem. **1966**, 5, 1466-1468.

25. A.K. Cheetham and B. E. F. Fender, "A powder neutron diffraction study of lanthanum and cerium trifluorides", Acta Cryst. **1976**, B32, 94-97.

26. R.P. Baumann and S.P.S. Porto, "Lattice vibrations and structure of rare-earth fluorides" Phys. Rev. **1967**, 161, 842-847.

27. C.D.E. Rango, G.vTsoucaris and C.C.R. Zelwer, Acad. Sci. Paris, Sdr. **1966**, C, 263, 64-66.

28. M. L. Afanasiev, S. P. Habuda and A. G. Lundin, "The symmetry and basic structures of LaF_3, CeF_3, PrF_3 and NdF_3" Acta Cryst. **1972**, B28, 2903-2905.

29. I. Brach, and H.Schulz, "Determination of the diffusion path in the ionic conductor LaF_3"

Solid State Ionics, **1985**, 15, 135-138.

30. B. Winkler, K. Knorr, and V. Milman, "Prediction of the structure of LaF_3 at high pressures" J. Alloys. Com. **2003**, 349, 111-113.

31. T.J. Udovic, Q.Z. Huang, A. Santoro, and J.J. Rush, "The nature of deuterium arrangements in Y D_3 and other rare-earth trideuterides", Zeitschrift fuer Kristallographie , **2008**, 223, 697-705.

32. M. Mansmann, "Zur kristallstruktur von lanthantrifluorid". Z. anorg. allg. Chem. **1964**, 331, 98–101.

33. A. Zalkin, D. H. Templeton, "The crystal structures of YF_3 andrelated compounds" J. Amer. Chem. Soc. **1953**, 75, 2453–2458.

34. M. Wang, Q. L. Huang, J. M. Hong, X.T. Chen, Z.L. Xue, "Selective synthesis and characterization of nanocrystalline EuF_3 with orthorhombic and hexagonal structures" Cryst. Grow. **2006**, Des. 6, 1972-1974.

35. Clegg, Robert. "The vital contributions of perrin and Förster. biophotonics int." **2004,** 43, 42-45.

36. P.R. Selvin, "Fluorescence resonance energy transfer" Meth Enzymol. **1995**, 246, 300-334.

37. Valuer, Bernard. "Molecular Fluorescence: Principles and Applications" Wiley - VCH, **2002**, 355-356.

38. F. Izumi, "The Rietveld Method,"ed. by R. A. Young, Oxford University Press, Chap. 13 (1993).

39. "The Rietveld Method,"ed. by R. A. Young, Oxford University Press, Chap. 13 (1993).

40. F. **Izumi** and T. **Ikeda**, "A Rietveld-analysis program RIETAN-98 and its applications to zeolites" Mater. Sci. Forum 2000**,** 198, 321–324.

Chapter 2. Analysis method of Eu^{3+} location in host matrix on the basis of $^5D_0$ decay

In general, doped RE ions can locate three sites in host LnF_3 crystal, one is substitution site (replacing Ln by Eu in LnF_3 lattice) with high symmetry, the other two with low symmetry are surface site (at the particles surface) and interstitial site (in LnF_3 lattice), both of them are called distorted site. Doped RE ion position in LnF_3 host strongly influences RE luminescence properties. In this Chapter, a new method to estimate the location of doped Eu^{3+} ions in host matrix is introduced. This method is based on the analysis of Eu^{3+} $^5D_0 \rightarrow {}^7F_{1,2}$ decay curves by least-square fitting method. This analysis method is illustrated by the case of $LaF_3:Eu^{3+}$ nanoparticles [1].

2.1 Experiment of $LaF_3:Eu^{3+}$ nanoparticles

Cetyltrimethylammonium bromide (CTAB, 99%) was obtained from SIGMA co.. All other reagents, $La(NO_3)_3.6H_2O$, NaF, and $EuCl_3.6H_2O$ from ALDRICH co., were used as received.

$LaF_3:Eu^{3+}$ nanoparticles have been synthesized by a hydrothermal method as shown in Figure 2-1. 5 mmol $La(NO_3)_3.6H_2O$, 0.25 mmol $EuCl_3.6H_2O$ and CTAB (0.006 mol/L) were dissolved in 150 mL deionized water. After being stirred mechanically for about 20 min. 15.75 mmol NaF was added drop by drop. A white suspension was gradually formed upon stirring. After stirred for 40 min. the mixture was transferred into a 250 mL autoclave, sealed, and heated at 140 °C for about 12 h. The system was then allowed to be cooled down to room temperature. The product was collected by centrifugation and washed subsequently with water and ethanol three times, respectively. After the centrifugation the particles were dried in an oven at 80 °C. The obtained nanocrystals were slowly calcined to 600 °C at a heating rate of 4 °C/min., annealed under a flow of N_2 gas for 2 h, and gradually cooled down to room temperature. The final product was a white powder of $La_{0.952}Eu_{0.048}F_3$ without CTAB.

The photoluminescence decay curves of $^5D_0 \rightarrow {}^7F_{1,2}$ transitions were recorded by a time-resolved photoluminescence (TRPL) system (Oriel Instruments, InstaSpec™ V system) under the excitation by

N_2 laser (USHO, KEC-160; λ_{ex} = 337.1 nm, pulse width < 1 ns). All of the experiments were done at room temperature.

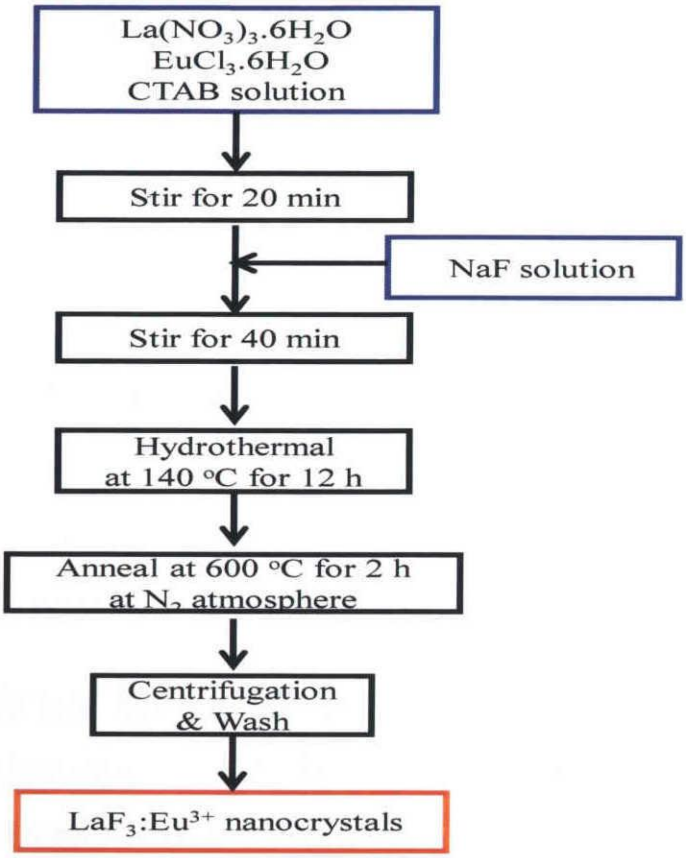

Figure 2-1 The flow chart of $LaF_3:Eu^{3+}$ nanoparticles preparation.

2.2 Results and discussion

2.2.1 PL spectrum and decay curves of Eu^{3+} ions $^5D_0$-$^7F_{1,2}$ transitions in $LaF_3:Eu^{3+}$

Room-temperature (RT) photoluminescence spectra (PL) was presented in Figure 2-2. The luminescence lines are assigned according to Carnells' paper [2]. As it was mentioned that Eu^{3+} ion is a good probe for the chemical environment of the lanthanide ion; the relative intensities of $^5D_0 \rightarrow {}^7F_1$ and $^5D_0 \rightarrow {}^7F_2$ emission, which are typical magnetic and electronic dipole transitions in character, respectively, depend strongly on the local symmetry of the Eu^{3+} ions [3]. In a site with inversion symmetry the $^5D_0 \rightarrow {}^7F_1$ magnetic dipole transition is dominant, while in a distorted site (without an inversion symmetry) the $^5D_0 \rightarrow {}^7F_2$ electric dipole transition is intensified in rate in comparison with the $^5D_0 \rightarrow {}^7F_1$ transition. In the emission spectra of $LaF_3:Eu^{3+}$ nanocrystals (see Figure 2-2), the dominating emission at 592 nm corresponds to the $^5D_0 \rightarrow {}^7F_1$ magnetic dipole transition, which indicates that Eu^{3+} ions were mainly located in a higher symmetric site close to an inversion symmetry in LaF_3 matrix. The peak at 619 nm can be ascribed to $^5D_0 \rightarrow {}^7F_2$ electric dipole transition, which is quite sensitive even to small changes in the chemical environment from an inversion symmetry surrounding Eu^{3+} ion. It is clear that the $I_{(5D0\rightarrow 7F2)}/I_{(5D0\rightarrow 7F1)}$ intensity ratio, called the asymmetry ratio, A, [3,4,5] give a measure of the local environment of the Eu^{3+} ion calculated about 0.310 indicating that Eu^{3+} ions occupied a higher symmetric site.

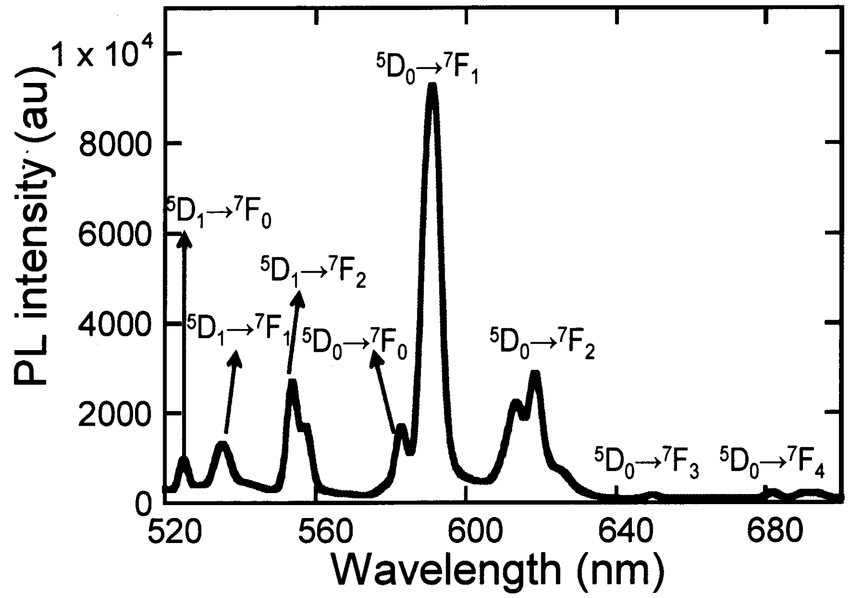

Figure 2-2 Photoluminescence spectra of $LaF_3:Eu^{3+}$ nanocrystals. (λ_{ex} = 397 nm).

Figure 2-3 shows the decay curves of the $^5D_0$-$^7F_1$ and $^5D_0$-$^7F_2$ luminescence monitored at 592 nm and 619 nm, respectively. As mentioned in Chapter 1, the photoluminescence decay curve of doped Eu^{3+} ions can offer the information on the change of the Eu^{3+} ligand structure [3] and on Eu^{3+} clusters [6]. We would like to start from an ideal system of Eu^{3+} ligand with a perfect inversion symmetry, in which electric dipole transitions such as $^5D_0$-$^7F_{2,4,6}$ are forbidden by a parity restriction of the *f-f* transitions (Laporte rule) [7], and negligible non-radiative effects. In the case, a dominant $^5D_0$ emission will be $^5D_0$-

$^7F_1$ of magnetic dipole, which is allowed by the selection rule $\Delta J = 0, \pm 1$ (except $0 \leftrightarrow 0$) via the following formula for a line strength [3],

$$S_{md} = \frac{e^2 h^2}{16\pi^2 m^2 c^2} \left| \langle f^N [\alpha SL] J \| L + 2S \| f^N [\alpha' S' L'] J' \rangle \right|^2 . \qquad \text{Eq.(2-1)}$$

It is known that S_{md} is independent of host material. The other transitions from $^5D_0$ to $^7F_{0,3,5}$ (owing to J-mixing) are very small. The $^5D_0$ lifetime is therefore determined by the magnetic dipole transition probability ($^5D_0$-^7F_J transition probability is denoted by $W_{0\text{-}J}$) [8],

$$W_{0\text{-}1} = A_{md} = \frac{64\pi^4 \nu^3}{3h(2J+1)} n^3 S_{md} , \qquad \text{Eq.(2-2)}$$

where ν is the wavenumber (cm^{-1}) of the transition and n is a refractive index of host material. The values corresponding to $^5D_0$-$^7F_1$ were given by several authors: Risefeld et al.[9] reported 9.4×10^{-8} as an oscillator strength. Axe et al. [10] obtained the transition probability of 43.3 sec^{-1} for europium ethylsulfate. C.Görller-Walrand et al. theoretically calculated magnetic dipole strengths [11] for $^5D_1$-$^7F_0$, $^5D_0$-$^7F_1$ and $^5D_2$-$^7F_1$. In $LaF_3:Eu^{3+}$ (n = 1.603) [12] the value of $W_{0\text{-}1}$ was obtained under the refractive index calibration and finally given to be 54.3 sec^{-1}, which contributes, of an order of tenth milli-seconds, to the $^5D_0$ lifetime.

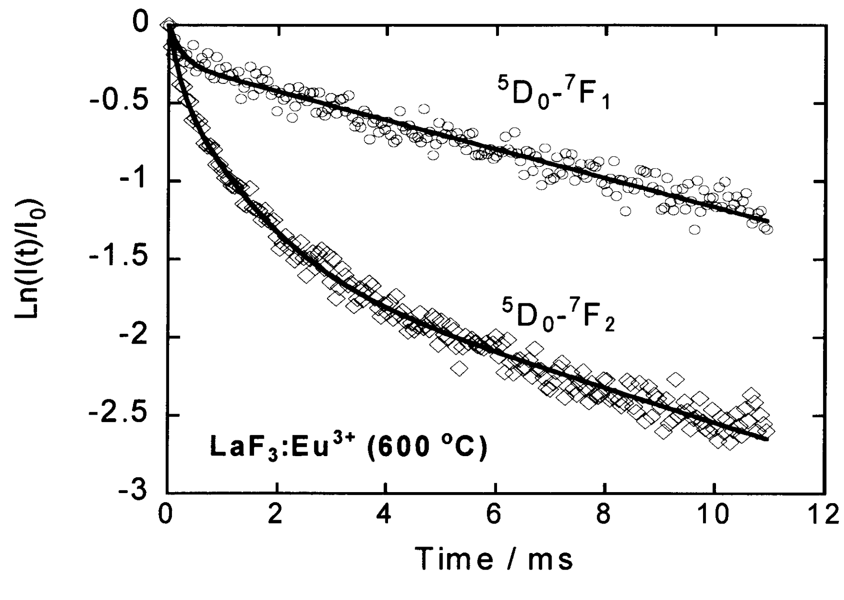

Figure 2-3 Decay curve of $^5D_0$-$^7F_{1,2}$ emission $LaF_3:Eu^{3+}$ nanocrystals The solid curves are obtained by a least-square fitting method.

However, in LaF_3 host there are the $^5D_0$-$^7F_1$ and $^5D_0$-$^7F_2$ transitions. It is due to the deviation from a perfect inversion symmetry but still an intense emission is given by $^5D_0$-$^7F_1$ ($\Lambda \sim 0.3$), that means the deviation is not very large. The other contributions of $^5D_0$-$^7F_0$ and $^5D_0$-$^7F_{3\text{-}6}$ are found to be very weak, as seen experimentally in the typical PL spectra of LaF_3:Eu^{3+}, and thus it can be accepted that these transition probabilities, $W_{0\text{-}0}$, $W_{0\text{-}3\sim6}$ are much less than $W_{0\text{-}1}$ and $W_{0\text{-}2}$. In the argument based on negligible non-radiative contribution to the $^5D_0$ lifetime in a host material with low phonon energy, the following equation is obtained for LaF_3:Eu^{3+},

$$1/\tau \sim W_{0-1} + W_{0-2} \qquad \text{Eq.(2-3)}$$

Strictly speaking, $W_{0\text{-}0}$ and $W_{0\text{-}3\sim6}$ have a few percentage of the contribution but is still small. $W_{0\text{-}2}$ is derived from odd terms of the ligand filed parameters, which is allowed as an electric dipole transition ruled by $\Delta J = 2$ and eventually result in the reduced $^5D_0$ lifetime via Eq.(2-3), of an order of a few milliseconds or submilliseconds. This is a basic status of our discussion. In the later part of this chapter, we shall focus on two transitions of $^5D_0$-$^7F_1$ and $^5D_0$-$^7F_2$ in our following analysis with a few percentages of errors.

Additionally, clustering of Eu^{3+} ions leads to shorten the Eu^{3+}-Eu^{3+} distances, fast energy transfer between Eu^{3+} ions, luminescence quenching combined with a killer site, and hence $^5D_0$ decay time shortening. If the clustering effect is not negligible, the above equation should be modified as followed,

$$1/\tau = W_{0\text{-}1} + W_{0\text{-}2} + W_{CL}. \qquad \text{Eq.(2-4)}$$

Such a non-radiative transition probability (W_{CL}) related with Eu^{3+} clustering influences the reduced $^5D_0$ lifetime as well. Thus, a longer $^5D_0$ decay time means that Eu^{3+} ions are better dispersed in a higher symmetric site and less clustered. The initial decay rate (τ_{init}) were determined within 1 ms of the $^5D_0 \rightarrow {}^7F_{1,2}$ decay curves and estimated as 10.8 ms and 2.6 ms for $^5D_0 \rightarrow {}^7F_1$ and $^5D_0 \rightarrow {}^7F_2$ emission, respectively.

The importance is that the lifetime observed is an order of 10 ms [13], which can be derived from Eu^{3+} ions in a higher symmetric site via Eq.(2-4) with negligible $W_{0\text{-}2}$ and W_{CL}.

2.2.2 Calculation of Eu^{3+} fraction in high symmetry site

In one site model for Eu^{3+} luminescence the time evolution of $^5D_0$ emission under pulsed excitation is expressed by single exponential function and moreover each of $^5D_0$-^7F_J PL must have the same lifetime inversely proportional to the summation of the different transition probabilities from the $^5D_0$ to different ^7F_J levels. This case is as long as the luminescence given from the same excited $^5D_0$ level. However, as seen in Figure 2-3, the experimental decay curves of $^5D_0$-$^7F_1$ and $^5D_0$-$^7F_2$ were not identically the same, it means that the Eu^{3+} luminescence should be explained with more than two sites for Eu^{3+} ions.

A simple way to do it is to apply a two-site model to the data of Figure 2-3, which can be analyzed with double exponential function [3] by a least-square fitting method:

$$I(t)/I_0 = \alpha \exp(-t/\tau_f) + \beta \exp(-t/\tau_s), \qquad \text{Eq(2-5)}$$

where τ_f is the decay time of the fast component, τ_s is the decay time of the slow component, and α and β is the amplitude ratio of the fast and slow components, respectively ($\alpha + \beta = 1$). Solid line in Figure 2-3 is the result of the fitting analysis for the LaF_3:Eu^{3+} nanocrystals. The fairly good fitting result is obtained for the $^5D_0$-$^7F_1$ decay curve. As for the $^5D_0$-$^7F_2$ decay, an additional exponential function is needed for the fast component in order to obtain the satisfactory result.

Table 2-1 summarizes the decay times in the $^5D_0$ luminescence analysis using the above-mentioned fitting procedure. The slow decay is characterized by 10 ms lifetime, which directly means a very small $^5D_0$-$^7F_2$ electric dipole transition probability, as mentioned in Section 3.3. The slow component must come from Eu^{3+} luminescence in a higher symmetric site (trigonal symmetric site for La^{3+}) of LaF_3 matrix. The lifetime for $^5D_0$ level is generally expressed by

$$1/\tau = W_{0\text{-}1} + W_{0\text{-}2} + W_{MP} + W_{CL}, \qquad \text{Eq.(2-6)}$$

Where $W_{0\text{-}1}$ is a magnetic dipole transition probability for $^5D_0$-$^7F_1$ transition while $W_{0\text{-}2}$ is an electric dipole transition probability for $^5D_0$-$^7F_2$ transition. For the LaF_3:Eu^{3+} nanocrystals heated at 600 °C, the mutiphonon relaxation probability W_{MP} (because of the lower phonon energy) and PL quenching probability due to Eu^{3+} clustering W_{CL} as non-radiative processes are negligible. Thus, the decay time τ_s of the slow component is approximately given through $1/\tau_s \sim W_{0\text{-}1}$. Here it has to be noted that the magnetic dipole probability $W_{0\text{-}1}$ of $^5D_0$-$^7F_1$ transition is almost constant, resulting from insensitiveness to chemical environments around Eu^{3+} ions. On contrary, the fast decay times (τ_{f1} and τ_{f2}) are as short as ~0.2 ms and ~1 ms, respectively. Such a short lifetime is observed for Eu^{3+} in distorted sites (surface site or interstitial site)

Table 2-1 Summary of decay curve analysis for the photoluminescence decay of $^5D_0$-$^7F_{1,2}$ emission for $LaF_3:Eu^{3+}$ nanocrystals heated at 600 °C.

	$^5D_0$-$^7F_1$ emission		$^5D_0$-$^7F_2$ emission		
	fast decay	slow decay	fast decay1	fast decay2	slow decay
Decay time / ms	0.220	10.7(9)	0.184	1.12	9.14
Amplitude, α, β	0.212	0.788	0.303	0.463	0.234
Luminescence Intensity	0.0466	8.49	0.0558	0.518	2.14
Relative Contribution	0.5(5) %	99.4(5) %	21.2%		78.8%
Intensity Ratio	0.005(5) ($=\eta_f$)	0.994(5) ($=\eta_s$)	0.065(6) ($=\xi_f$)		0.244(4) ($=\xi_s$)
	1.00 ($= \eta_f + \eta_s$)		0.310 *1) ($= \xi_f + \xi_s$)		
Microscopic Λ			$\Lambda_{fast} = 12.0$ *2)		$\Lambda_{slow} = 0.25$ *3)
W_{0-2}			$W_{0-2}^{dis} = 12.0W_{0-1}$		$W_{0-2}^{hs} = 0.25W_{0-1}$

*1) corresponding to the apparent asymmetric ratio Λ of 0.31 obtained from the luminescence spectrum in Figure 2-2.
*2) $\Lambda_{fast} = \xi_f / \eta_f$,
*3) $\Lambda_{slow} = \xi_s / \eta_s$

The luminescence intensity can be calculated from multiplexing the decay time (ex. τ_f) with the corresponding amplitude (ex.α), which is also given in Table 2-1($\eta_f = \tau_f \times \alpha$, $\eta_s = \tau_s \times \beta$ for $^5D_0$-$^7F_1$; $\xi_f = \tau_f \times \alpha$, $\xi_s = \tau_s \times \beta$ for $^5D_0$-$^7F_2$). Figure 2-4 displays respective contributions of Eu^{3+} ions in different PL characters ($\eta_{f,s}$ and $\xi_{f,s}$ in Table 2-1) to $^5D_0$-$^7F_{1,2}$ luminescence intensities for the $LaF_3:Eu^{3+}$

nanocrystals heated at 600 °C, which had the stronger luminescence intensity and the apparent lower asymmetric ratio A of 0.310. As a result of the decay analysis, it can be seen that the over-all luminescence intensities come from two different phosphorous sites of Eu^{3+} ions. One is a higher (trigonal) symmetric site in LaF_3 nanocrystal and the other is a much distorted site probably located at the surface of LaF_3 nanocrystals as described in Chapter 3. Additionally, we can calculate a microscopic asymmetric ratio, A value, for each of inversion symmetric and distorted sites. The former has a value of 0.25, a little bit smaller than the apparent (macroscopic) A of 0.31, and the latter has 12.0 (see Table 2-1 and Figure 2-4).

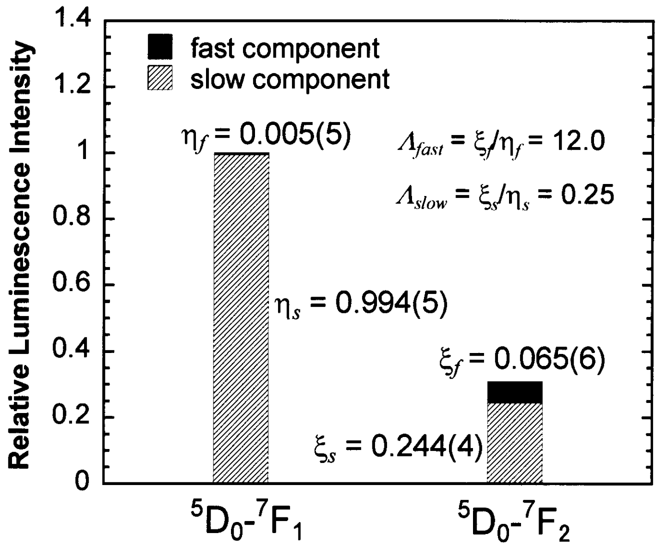

Figure 2-4 Relative luminescence intensity of $^5D_0$-$^7F_{1,2}$ peak at 592 and 619 nm, respectively. The intensities can be decomposed with the fast and slow decay components given by the decay curve analysis

As it has been mentioned that the life times for $^5D_0$ level can be expressed by (see Eq. 2-6)

$$1/\tau = W_{0\text{-}1} + W_{0\text{-}2} \qquad \text{Eq. (2-6)}$$

so the life times from disordered site and high symmetric site for $^5D_0$ level expressed as follows

$$\frac{1}{\tau^{\mathrm{dis}}} = W_{0-1} + W_{0-2}^{\mathrm{dis}} \qquad \text{Eq. (2-7)}$$

and

$$\frac{1}{\tau^{\mathrm{hs}}} = W_{0-1} + W_{0-2}^{\mathrm{hs}} \qquad \text{Eq. (2-8)}$$

In Table 2-1 it was estimated that W_{0-2}^{dis}=12.0×$W_{0\text{-}1}$ and W_{0-2}^{hs}=0.25×$W_{0\text{-}1}$, the Eq.(2-7) and Eq.(2-8) could be modified as

$$\frac{1}{\tau^{\mathrm{dis}}} = 13.0 \times W_{0-1} \qquad \text{Eq. (2-9)}$$

and

$$\frac{1}{\tau^{\mathrm{hs}}} = 1.25 \times W_{0-1} \qquad \text{Eq. (2-10)}$$

from the fitting result, it is known that τ^{hs}=10.8 ms (see Table 2-1), W_{0-1}can be calculated and the value was as 74.07 sec^{-1}, it was according well with the value (54.3 sec^{-1}) reported by C.Görller-Walrand group [11]. Taking into account the W_{0-1}= 74.07 sec^{-1} in Eq.(2-9), τ^{dis} value was obtained and the value was about 1.0 ms, this value was coincided with the experimental data of the fast component of the lifetime (1.12 ms), it could be confirmed that the fitting result was reliable.

The large asymmetric ratio A = 12.0 indicates that the reduced $^5D_0$ lifetime of the fast component isn't a result from symmetric Eu^{3+} in Eu cluster accompanying with PL quench. Furthermore, this microscopic consideration on Eu^{3+} sites located in LaF_3 nanocrystals allows us to estimate the fractional number N of Eu^{3+} ions in a higher (trigonal) symmetric or distorted site. The luminescence intensity is proportional to

$$N \times \frac{W_{0-1}}{W_{0-1} + W_{0-2}} \qquad \text{Eq.(2-11)}$$

and

$$N \times \frac{W_{0-2}}{W_{0-1} + W_{0-2}} \qquad \text{Eq.(2-12)}$$

for $^5D_0$-$^7F_1$ and $^7F_2$ luminescence lines, respectively. For a higher (trigonal) symmetric site, an electric dipole transition probability $W_{0\text{-}2}$, denoted by $W_{0\text{-}2}{}^{hs}$, is closer to zero or very small (the factor of 0.25 in comparison with $^5D_0$-$^7F_1$ intensity) and so the $^5D_0$-$^7F_1$ luminescence intensity is approximately given by N^{hs},

$$I^{hs} \propto N^{hs} \times \frac{W_{0-1}}{W_{0-1} + W_{0-2}{}^{hs}} \cong N^{hs} \qquad \text{Eq.(2-13)}$$

One the other hand, Eu^{3+} ions in a distorted site have a considerable value of $W_{0\text{-}2}$, denoted by $W^{dis}{}_{0\text{-}2}$, which can be calculated from the microscopic Λ value, $\Lambda_{\text{fast}} = W^{dis}{}_{0\text{-}2} / W_{0\text{-}1} = \xi_f / \eta_f$. Hence, $W_{0\text{-}2}{}^{dis} = 12.0\ W_{0\text{-}1}$ for a distorted site. The $^5D_0$-$^7F_1$ luminescence intensity of Eu^{3+} ions in a distorted site is calculated to be

$$I^{dis} \propto N^{dis} \times \frac{W_{0-1}}{W_{0-1} + W_{0-2}{}^{dis}} = N^{dis} / 13.0 \qquad \text{Eq.(2-14)}$$

The similar calibration must be applied in Eq.(2-11) for a higher (trigonal) symmetric site. Since $W_{0\text{-}2}{}^{hs} = 0.25 W_{0\text{-}1}$ from $\Lambda_{\text{slow}} = 0.25$ (see Table 2-1),

$$I^{hs} \propto N^{hs} \times \frac{W_{0-1}}{W_{0-1} + W_{0-2}{}^{hs}} = N^{hs} / 1.25 \qquad \text{Eq.(2-15)}$$

I^{hs} and I^{dis} are proportionally related with η_s and η_f, respectively, given in Table 2-1 and Figure 2-4 and therefore we can estimate the fractional number of Eu^{3+} ions in each site in the LaF_3 nanocrystal. According to the results in Table 2-1, it can finally be concluded that 94.6 percentage (%) of Eu^{3+} ions occupies a higher (trigonal) symmetric site while the other is in distorted sites (the detail is given in Table 2-1 and Table 2-2). At the present time, the distorted sites for Eu^{3+} are speculated to be on the surface of LaF_3 nanocrystals. Figure 2-5 shows the low temperature (9 K) PL spectra of LaF_3:Eu^{3+} ions excited at 578.4 nm. The directed excited spectra has a very high microscopic asymmetric ratio value ($\Lambda \approx 10$), which elucidated that the Eu^{3+} ions located at very distorted sites were potentially excited and the Λ value of Eu^{3+} luminescence intensity ratio come from distorted sites estimated in decay curves analysis was valid.

Table 2-2 Estimation of the fractional number of Eu^{3+} ions in LaF_3 lattice

	Higher (trigonal) symmetric site	Disturbed site
Microscopic Λ	0.25	12.0
$I(^5D_0$-$^7F_1)$	N^{hs} / 1.25	N^{dis} / 13.0
$\eta_{s,f}$	0.995(5)	0.005(5)
$N^{hs,\ dis}$	94.6 %	5.4 %

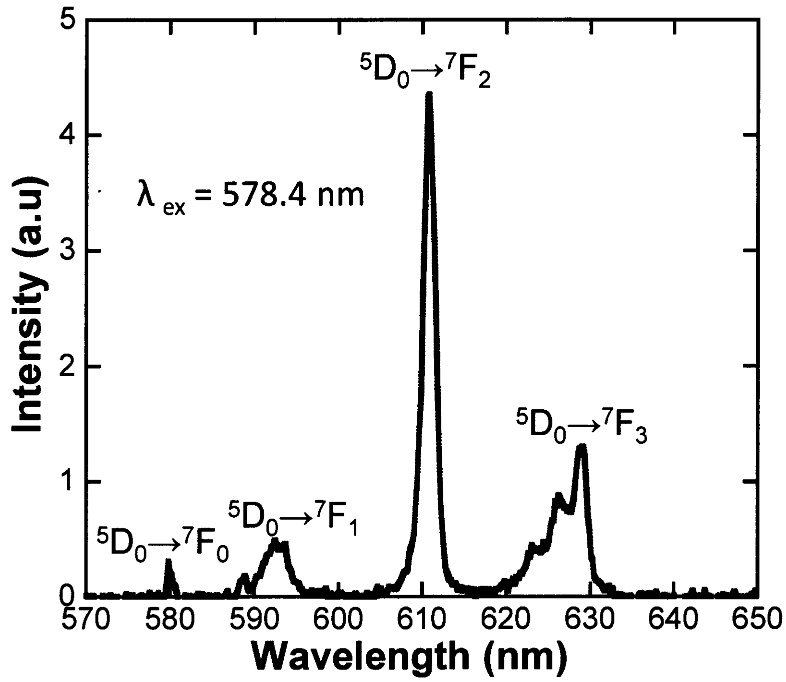

Figure 2-5 Low temperature (9 K) photoluminescence spectra of $LaF_3:Eu^{3+}$ nanocrystals. (λ_{ex} = 578.4 nm).

2.3 Conclusion

In this section, the method of analysis Eu^{3+} located position in host matrix has been illustrated by the case of Eu^{3+} ion doped in LaF_3 nanocrystals,. In this method Eu^{3+} $^5D_0$-$^7F_{1,2}$ decay curves were fitted by a least-square method and analyzed using double exponential functions. According to the fitting result, a fraction of Eu^{3+} located in different site can be estimated. This method was used throughout this thesis and should be a useful method in rare-earth doped luminescence materials.

2.4 References

1. X. T. Zhang, T. Hayakawa, M. Nogami, "Photoluminescence properties and $^5D_0$ decay analysis of $LaF_3:Eu^{3+}$ nanocrystals prepared by using surfactant" Int. J. Appl.Ceram.Tech. **2009**, in press.

2. W. T. Carnall, P. R. Fields and K. Rajnak, "Electronic energy levels of the trivalent lanthanide aquo ions. IV. Eu^{3+}", J. Chem. Phys. **1968**, 49, 4450-4455.

3. R. D. Peacock, "The intensity of lanthanide f-f transition", in *Structure and Bonding,* Vol.22, edited by J. D. Duruitz, P. Hemmerih, R. H. Holm, J. A. Ibers, C. K .Jorgenson, J. B. Neiland, D. Reinen and R. J. P. Williams (Springer, Berlin, 1975).

4. J.H. Kim and P.H. Holloway, "Room-temperature photoluminescence and electroluminescence properties of sputter-grown gallium nitride doped with europium", J. Appl. Phys. **2004,** 95, 4787-4790.

5. L. Chen, Y. Liu and Y. Li, "Preparation and characterization of $ZrO_2:Eu^{3+}$ phosphors" J. Alloys. Comp. **2004**, 381, 266-271.

6. T. Hayakawa and M. Nogami, "Energy migration of the local excitation at the Eu^{3+} site in a Eu-O chemical cluster in sol-gel derived $SiO_2:Eu^{3+}$ glasses" J. Appl. Phys. **2001**, 90, 2200-2205.

7. O. Laporte and W.F. Meggers, "Some rules of spectral structure", J. Opt. Soc. Am. **1925,** 11, 459-460.

8. C. Görller-Walrand and K. Binnemans, in: K. A. Gschneidner Jr. and L. Eyring (Eds.), "Handbook on the Physics and Chemistry of Rare Earths", vol.25, North-Holland, Amsterdam, 1998 (Chapter 167).

9. R. Reisfeld, E. Greenberg, R. N. Brown, M. G. Drexhage and C.K. Jorgensen, "Fluorescence of europium (III) in a fluoride glass containing zirconium", Chem. Phys. Lett. **1983**, 95, 91-94.

10. J. D. Axe, JR, "Radiative transition probabilities within 4/n configurations: the fluorescence spectrum of europium ethylsulphate" J. Chem. Phys. **1963**, 39, 1154-1160.

11. C. Görller-Walrand, L. Fluyt, A. Ceulemans and W. T. Carnall, "Magnetic dipole transitions as standards for judd-ofelt parametrization in lanthanide spectra" J. Chem. Phys. **1991**, 95, 3099-3106.

12. M. Bass (Ed.), "Handbook of Optics", vol. 2, 2nd edition, McGraw-Hill, 1994.

13. T. Hayakawa and M. Nogami, "High luminescence quantum efficiency of Eu^{3+}-doped SnO_2-SiO_2 glasses due to excitation energy transfer from nano-sized SnO_2 crystals" Sci. Tech. Adv. Mater. **2005**, 6, 66-70.

Chapter 3. Effect of LaF_3 particle size on luminescence properties of doped Eu ion

In this chapter, size tuned $LaF_3:Eu^{3+}$ nanocrystals in hexagonal phase have been synthesized by a hydrothermal method with CTAB as a size-controlling agent. Different size samples were well characterized by X-ray diffraction (XRD) analysis, transmission electron microscopy (TEM), photoluminescence excitation and emission spectral measurements. Sample synthesized with 0.006 mol/L CTAB and annealed at 600 °C with larger particle size and exhibited stronger Eu^{3+} luminescence intensity than other samples. The correlation between particle size and luminescence properties were discussed in this chapter [1,2].

3.1 Introduction

Lanthanum trifluoride LaF_3 [3,4,5] is an ideal host material for various phosphors because this material has very low phonon energy (~350 cm^{-1}) [4], thus the multi-phonon relaxation of the excited state of rare-earth ions doped can be minimal. The preparation and luminescence of $LaF_3:Eu^{3+}$ nanoparticles have been reported by several authors [6,7,8,9,10,11]. J.-X. Meng et al.[11] used $La(NO_3)_3$, $Eu(NO_3)_3$ and NH_4F as reactants to synthesize $LaF_3:Eu^{3+}$ nanoparticles. Both $La(NO_3)_3$ and NH_4F is dissolvable significantly in water, while LaF_3 is an insoluble salt in water, so that solid LaF_3 precipitations can easily be obtained by the reaction of La^{3+} and F^- ions formed by the dissociation of $La(NO_3)\cdot 6H_2O$ and NH_4F in an aqueous solution. However, since high La^{3+} and F^- ions concentration in an aqueous solution resulted in significantly high reaction rates, it is difficult to control the growth of LaF_3 crystalline. In materials science on nanophosphors, it is known that the size of very fine particles greatly influenced their luminescence properties. In this section, size tuned $LaF_3:Eu^{3+}$ nanocrystals were synthesized via a hydrothermal method by using cethyltrimethylammonium bromide (CTAB) as an additive to control the particle growth. The influences of post-annealing temperature and CTAB concentration on the particles size as well as on the photoluminescence (PL) properties were studied. Particle size effects on doped Eu ions luminescence properties were discussed. It was found that in large particles doped Eu ions prefer to locate in high symmetric site which induced strong luminescence intensity. $LaF_3:Eu^{3+}$ nanoparticles growth mechanism also discussed in this section.

3.2 Experiment of size tunable $LaF_3:Eu^{3+}$ nanoparticle

$LaF_3:Eu^{3+}$ nanoparticles were prepared by the same procedures described in experiment of $LaF_3:Eu^{3+}$ nanoparticles section of Chapter 2. In order to get particles with different size, CTAB concentration was changed from to 0 mol/L, 0.006 mol/L, 0.009 mol/L to 0.015 mol/L, post-annealing temperature was varied from 500 °C, 600 °C, 700 °C to 800 °C.

The crystalline data were obtained by X-ray diffractometer (XRD: Phillips X`pert system using Cu K_{α}; 45 kV, 40 mA). The data was collected by scanning between 2θ = 20 and 75 ° in 0.02 ° steps. Transmission electron microscopy (TEM) observation was done with a JEM-2010HR microscope (JEOL). The photoluminescence excitation (PLE) and photoluminescence (PL) spectra were obtained with F-7000 fluorescence spectrophotometer (Hitachi, co.). The photoluminescence decay curves of $^5D_0 \rightarrow {}^7F_{1,2}$ transitions were recorded by a time-resolved photoluminescence (TRPL) system (Oriel Instruments, InstaSpec^{TM} V system) under the excitation by N_2 laser (USHIO, KEC-160; ë$_{ex}$ = 337.1 nm, pulse width < 1 ns). All of the experiments were carried out at room temperature.

3.3 Results and discussion

3.3.1 $LaF_3:Eu^{3+}$ nanoparticles size analysis as the function of CTAB concentration

Figure 3-1 shows the variation of XRD pattern of samples depending on CTAB concentration. The good agreement of diffraction peak positions with the PDF Card No. 82-0684, indicates that the $LaF_3:Eu^{3+}$ synthesized is in hexagonal structure [11]. From Figure 3-1, it can be found that a sample synthesized with 0.006 mol/L CTAB has the higher and sharper peaks than those with other CTAB concentrations. Particle size of the sample were estimated by applying the Scherrer formula to the full width at half maximum (FWHM) of the (111) diffraction peak. The calculated particle sizes indicated in Figure 3-2 shows, it reaches to maximum value when 0.006mol/L CTAB is used. The largest $LaF_3:Eu^{3+}$ particles were obtained with 0.006 mol/L CTAB concentration.

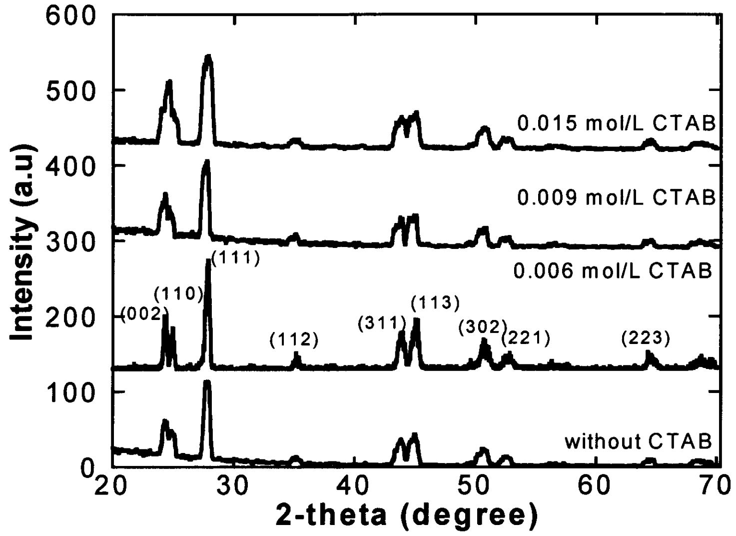

Figure 3-1 X-ray diffraction patterns of $LaF_3:Eu^{3+}$ nanocrystals synthesized with different CTAB concentrations. All the samples were heated at 600 °C.

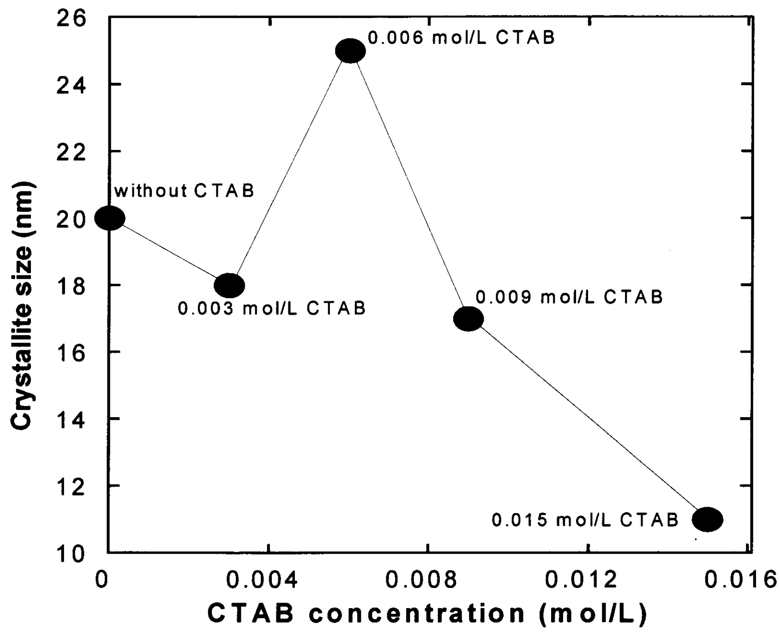

Figure 3-2 Crystallite size of $LaF_3:Eu^{3+}$ nanoparticles synthesized with different CTAB concentrations, calculated with Scherrer's equation.

3.3.2 $LaF_3:Eu^{3+}$ nanoparticle size analysis as the function of annealing temperature

Figure 3-3 shows the variation of XRD pattern of samples depending on the annealing temperature. The diffractive peak positions also are in good agreement with the PDF Card No. 82-0684. From Figure 3-3 it can be found that a sample heated at 600 °C exhibited the higher and sharper peaks. When heated at 800 °C a small tiny peak near the (111) peak could be found. The small tiny peak was the (101) diffractive peak of LaOF (PDF Card No. 86-2377) phase. This is thought to result from partial oxidation of the LaF_3 nanoparticals, which is due to oxygen residues in the products. So the sample synthesized with 0.006 mol/L CTAB and heated at 600 °C has the good crystalline structure.

Figure 3-4 shows the crystallite size of the nanoparticles heated at different temperatures. The crystallite size was increased with increasing calcination temperatures up to 600 °C and once decreased down at 700 °C. However, at higher temperature the size was again increased. The crystallite size of the sample heated at 600 °C was calculated as 25.4 nm and for the sample heated at 800 °C was 32.6 nm.

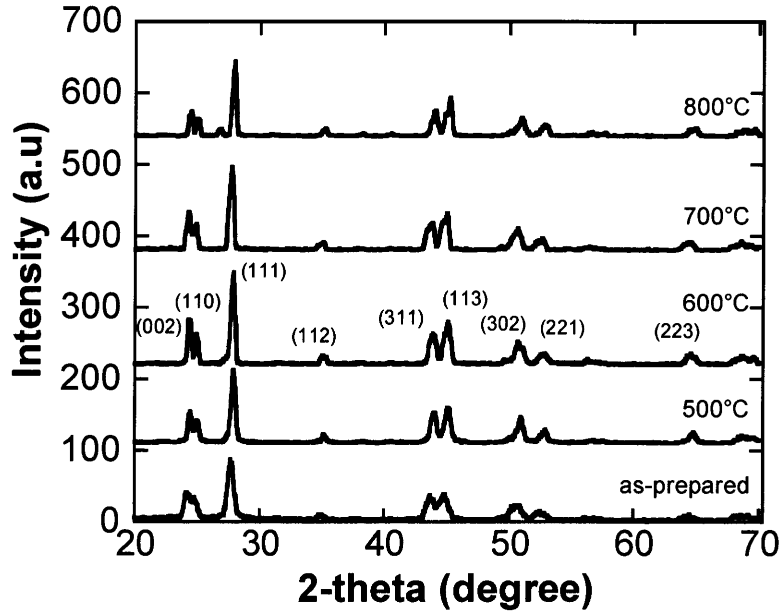

Figure 3-3 X-ray diffraction patterns of $LaF_3:Eu^{3+}$ nanocrystals heated at different temperatures. All the samples were synthesized with 0.006 mol/L CTAB.

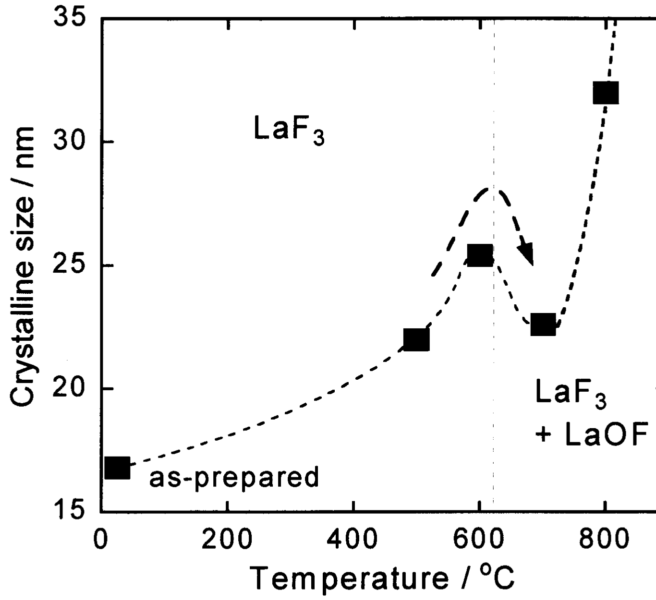

Figure 3-4 Crystallite size of $LaF_3:Eu^{3+}$ nanoparticles heated at different temperatures, calculated with Scherrer's equation.

3.3.3 Particle growth mechanism

CTAB is a kind of cationic surfactants consisting of a polar hydrophilic head group and a non-polar hydrophobic tail as shown in Figure 3-5. The synthesis scheme of $LaF_3:Eu^{3+}$ nanocrystals with aid of CTAB molecules is shown in Figure 3-6. When the concentration of CTAB was more than critical micelle concentration (CMC), corresponding to be about 0.006 mol/L in this experiment, a micelle structure begins to be formed where the size and morphology of CTAB micelle are influenced by CTAB concentration pH and salts [12,13,14]. On the other hand, a lot of $LaF_3:Eu^{3+}$ nucleus seeds were at first produced after the addition of NaF into the mixture of La^{3+}/Eu^{3+} aqueous solution (see 3.2) and adsorbed by the hydrophobic tail of CTAB and finally located inside CTAB micelle. These $LaF_3:Eu^{3+}$ nucleus seed can be served as nucleation centers, which was allowed to grow into $LaF_3:Eu^{3+}$ single crystal (explained below) with an appropriate size in the hydrothermal process in autoclave. On the contrary, when the CTAB concentration is more than CMC, the number of CTAB micelles increases with the diameter of CTAB micelle decreased. And then the average number of LaF_3 nucleus seeds situated in a CTAB micelle will be decreased. Less nucleus seeds served as nucleation centers in a

CTAB micelle do not permit $LaF_3:Eu^{3+}$ to grow into a larger particle. This is why as the CTAB concentration increased the particle size was decreased.

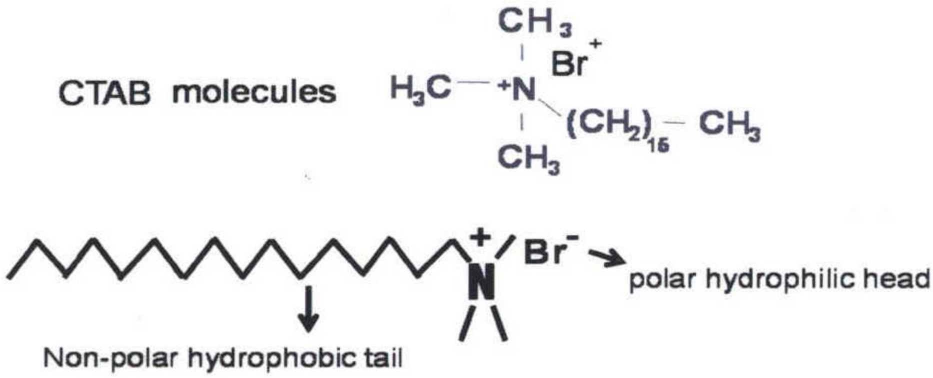

Figure 3-5 CTAB molecule configuration.

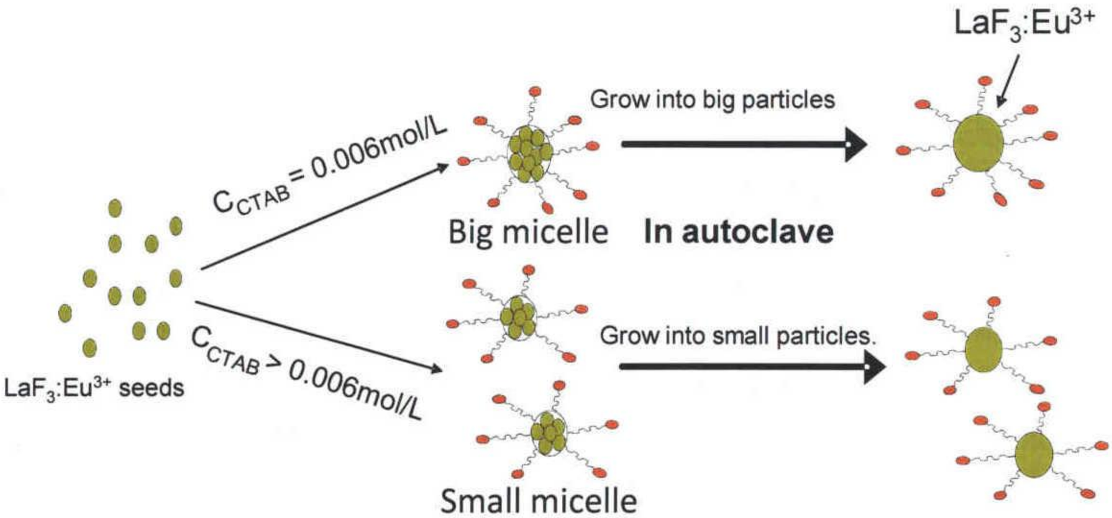

Figure 3-6 Synthesis scheme of $LaF_3:Eu^{3+}$ nanocrystals in CTAB micelles.

3.3.4 TEM images and Selected Area Electron Diffraction (SAED) pattern of $LaF_3:Eu^{3+}$ synthesized with 0.006 mol/L CTAB concentration

Figure 3-7 shows TEM image of $LaF_3:Eu^{3+}$ nanocrystals synthesized with 0.006 mol/L CTAB and heated at 600 °C. The photograph shows that particle diameter was in the range of 20-30 nm and dispersed well. It is well corresponding to the value calculated by Scherrer formula from the XRD data.

The inset is selected area electron diffraction (SAED) pattern of $LaF_3:Eu^{3+}$ nanocrystal, indicating that it had a single crystal structure with hexagonal symmetry.

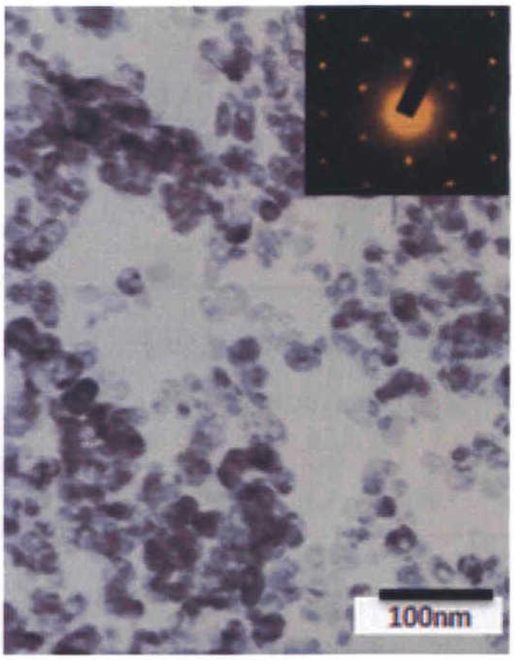

Figure 3-7 TEM image and selected area electron diffraction pattern of sample synthesized with 0,006 mol/L CTAB and annealing at 600 ^{O}C.

3.3.5 Size distribution analysis of $LaF_3:Eu^{3+}$ particles synthesized with 0.006 mol/L CTAB

From TEM image shown in Figure 3-7, we analyzed size-distribution of $LaF_3:Eu^{3+}$ nanocrystals (Figure 3-8). It was found that the sample had a narrow size distribution and ~81% particles within the diameter range of 20~30 nm. It is well corresponding to the value calculated by Scherrer formula from the XRD data.

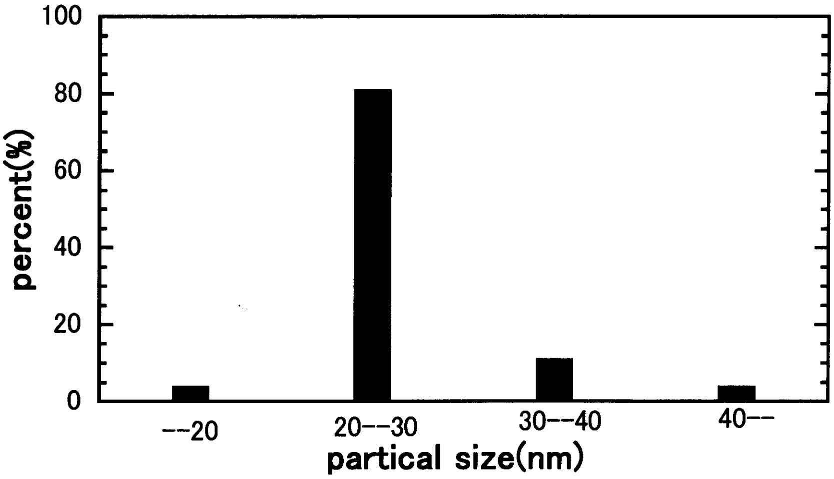

Figure 3-8 Size-distribution of $LaF_3:Eu^{3+}$ particles synthesized with 0.006 mol/L CTAB.

3.3.6 Photoluminescence spectra

Room-temperature photoluminescence spectra of samples synthesized with different CTAB concentration and annealing at different temperature are presented in Figure 3-9 and Figure 3-10, respectively. The luminescence lines are assigned according to Carnell's paper [15]. The dominating emission at 592 nm corresponds to the $^5D_0 \rightarrow {}^7F_1$ magnetic dipole transition. The peak at 619 nm can be ascribed to $^5D_0 \rightarrow {}^7F_2$ electric dipole transition. Because of very low phonon energy of LaF_3 crystal, luminescence form higher excited state of $^5D_1$ was also observed (See the region from 500 to 700 nm in). When the Eu^{3+} ion located in a La^{3+} site with C_2 symmetrythe electric and magnetic dipoles are allowed. Therefore, both the $^5D_0 \rightarrow {}^7F_1$ and the $^5D_0 \rightarrow {}^7F_2$ transitions of Eu^{3+} can be observed in $LaF_3:Eu^{3+}$ nanocrystals, this is also the reason why LaF_3 was selected as host in this study. The strongest Eu^{3+} luminescence was $^5D_0$-$^7F_1$ transition because of the site symmetry of La^{3+} in LaF_3 lattice. Figure 3-9 clearly shows that the sample synthesized with 0.006 mol/L CTAB exhibited about 1.5 times higher $^5D_0$-$^7F_1$ luminescence than without CTAB. On the other hand, for more CTAB concentration, the Eu^{3+} luminescence was monotonically decreased with increasing CTAB concentration. Figure 3-10 shows that heating at 600 °C increases PL intensity of $LaF_3:Eu^{3+}$ nanocrystals about twice.

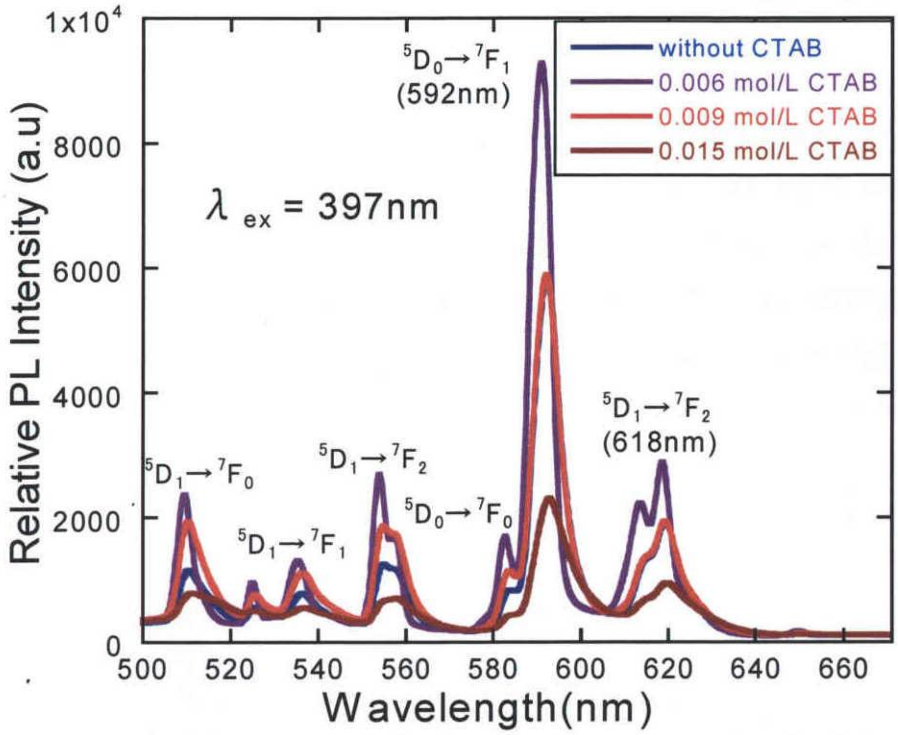

Figure 3-9 PL spectra of $LaF_3:Eu^{3+}$ nanocrystals with different CTAB concentrations (λ_{ex} = 397 nm). The all samples were annealed at 600 °C.

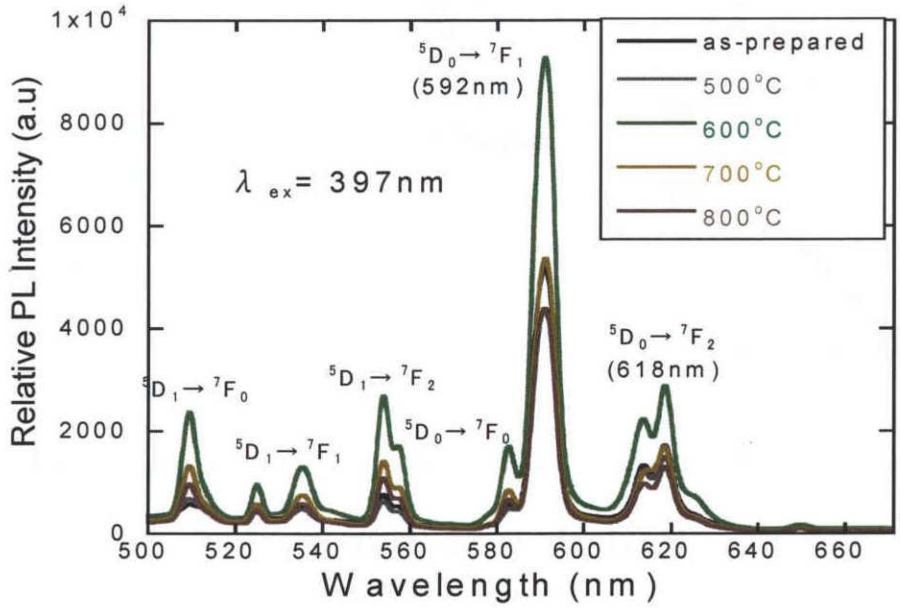

Figure 3-10 PL spectra of samples heated at different temperatures (λ_{ex} = 397 nm). The all samples were synthesized with 0.006 mol/L CTAB.

3.3.7 Correlation between particle size and luminescence intensity

As discussed above, the particle size was increased with increasing calcination temperature up to 600 °C, and once decreased down at 700 °C and then increased again. $LaF_3:Eu^{3+}$ nucleus grew into large particles (about 25 nm) by a help of CTAB micelle structure at 0.006 mol/L CTAB concentration, but $LaF_3:Eu^{3+}$ particle size was decreased by more increase of CTAB concentration. Figure 3-11 shows the $LaF_3:Eu^{3+}$ luminescence intensity as the function of particle size. It was found that Eu^{3+} ions luminescence intensity was increased with the particle size except for the sample annealed at 800 °C. At 800 °C the particle size is largest however partial oxidations of the LaF_3 nanoparticles occurred and surface defects on $LaF_3:Eu^{3+}$ nanoparticles were produced. So it was confirmed that the large particle exhibited strong luminescence intensity regardless of CTAB concentration and annealing temperature if the oxidation did not occur.

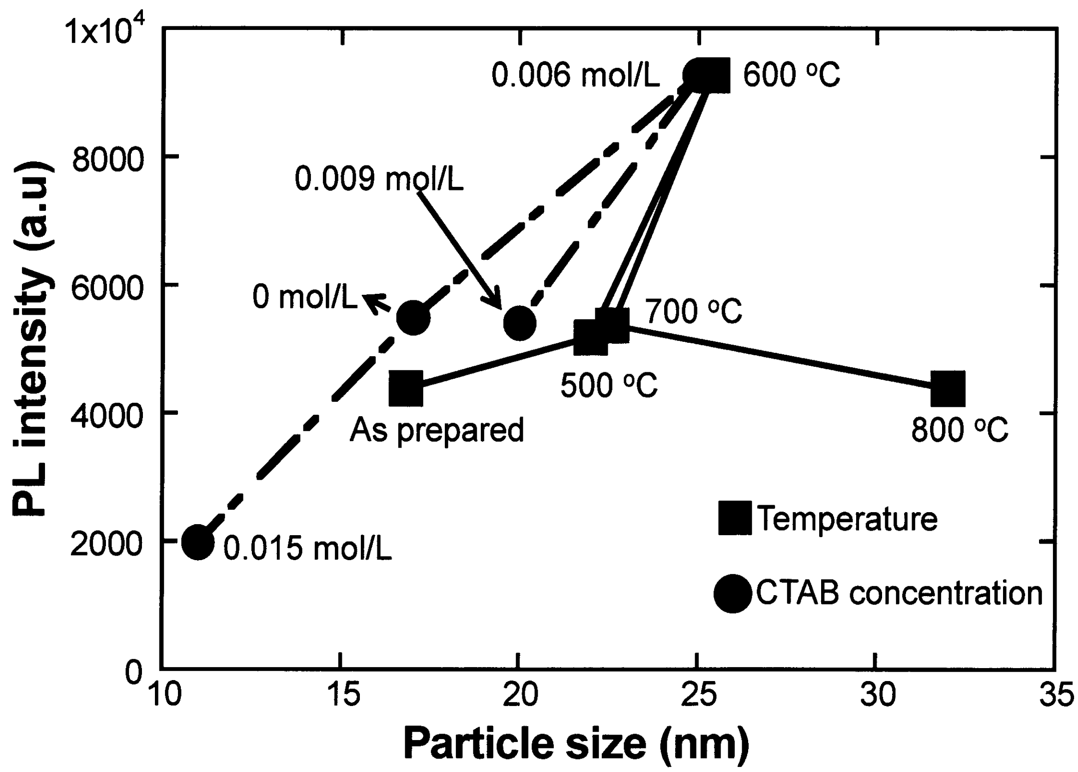

Figure 3-11 Intensity of the 592 nm emission of $LaF_3:Eu^{3+}$ nanocrystals as a function of particle size.

3.3.8 Decay curves of samples synthesized with different CTAB concentration

$^5D_{0\text{-}1}$ and $^5D_{0\text{-}2}$ Luminescence decay curves of Eu in samples synthesized with different CTAB concentrations were shown in Figure 3-12 and Figure 3-13 respectively. Black lines are fitting results of decay curves. The initial decay rates (τ_{init}) are determined within 1.5 ms of the decay curves, as displayed in Table 3-1. The sample synthesized with 0.006 mol/L CTAB has a long lifetime for $^5D_0$ level, it means that Eu^{3+} ions are well dispersed with high symmetric site in the nanocrystals synthesized with 0.006mol/L CTAB and heated at 600 °C. This eventually leads to the stronger luminescence.

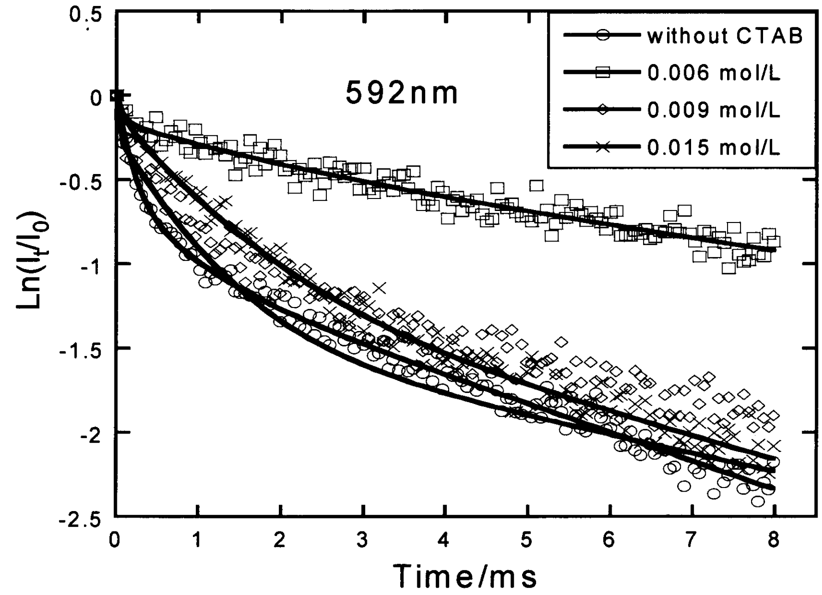

Figure 3-12 Variation of $^5D_0 \rightarrow {}^7F_1$ photoluminescence decay curves of Eu^{3+} fluorescence of samples depending on the CTAB concentration. The excitation and monitoring wavelength are 337.1 nm and 592 nm, respectively.

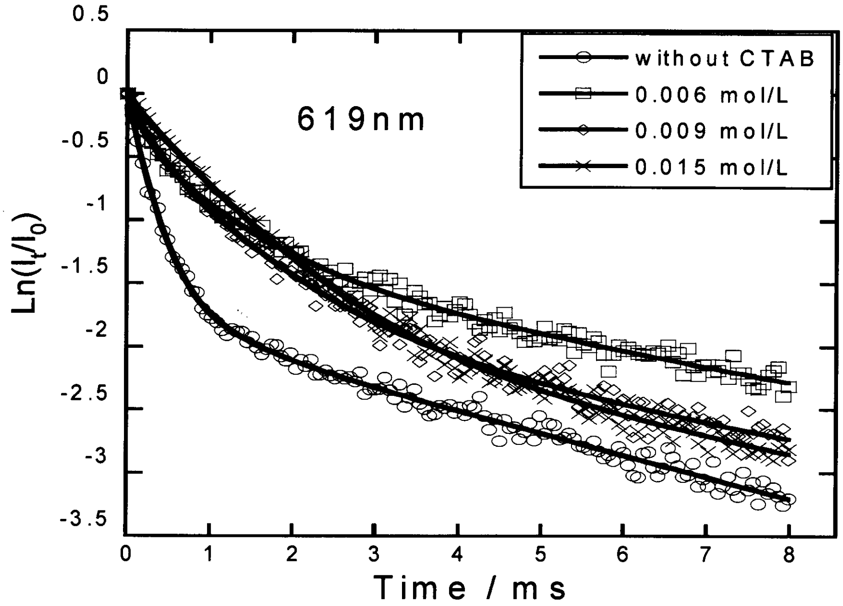

Figure 3-13 Variation of $^5D_0 \rightarrow {}^7F_2$ photoluminescence decay curves of Eu^{3+} fluorescence depending on CTAB concentration. The excitation and monitoring wavelength are 337.1 nm and 619 nm, respectively.

Table 3-1 Initial decay times τ_{init} of $^5D_0$-^7F_J (J = 1, 2) emission for $LaF_3:Eu^{3+}$ nanocrystals synthesized with different CTAB concentrations.

CTAB concentration	$^5D_{0\text{-}1}$ (at 592 nm)	$^5D_{0\text{-}2}$ (at 619 nm)
0 mol/L	1.26 ms	0.70 ms
0.006 mol/L	10.8 ms	2.60 ms
0.009 mol/L	1.54 ms	1.22 ms
0.015 mol/L	1.73 ms	1.43 ms

3.3.9 Estimation of Eu ion fraction in high symmetric site

In Chapter 2, a new method to analyze Eu ion location in host matrix was introduced. Accordin to this method possible positions of Eu^{3+} ions located in LaF_3 matrix could be estimated from decay curve fitting results. The same methodology is applied and the estimations are summarized in Table 3-2. The fractional number of Eu^{3+} ions in higher symmetric site-substitution site in LaF_3 lattice matrix is obviously affected by CTAB concentration. After CTAB concentration reaches to 0.006 mol/L, it gets the maximum value of about 95%, and then decreases quickly with increasing CTAB concentration. This is because when the concentration of CTAB is more than critical micelle concentration (CMC), corresponding to about 0.006 mol/L in this experiment, a micelle structure begins to be formed, micelle helps synthesize large and well dispersed crystals. Figure 3-14 shows that with an increasing of CTAB concentration, Eu fraction in high symmetric site variation shows the same tendency as particle size. In the other word, large particle has the large Eu fraction in a high symmetric site. As shown in Figure 3-15, the fact that Eu luminescence intensity increased as surface/volume ratio decreased allows us to conclude that Eu ions distorted site is in the surface-state site, and thus the decreasing particle size must reduce the Eu^{3+} luminescence since surface/volume ratio ($\propto$ 1/D) is increased and surface defects more greatly exhaust excitation energy of Eu^{3+} ions doped in LaF_3 nanocrystals. In Chapter 2, it was mentioned that $^5D_0 \rightarrow {}^7F_2$ emission decay curves was fitted by three exponential function, decay lifetime of the two fast components of $^5D_0 \rightarrow {}^7F_2$ emission are 0.184 ms and 1.12 ms, so much short lifetimes are also confirmed that Eu ions distorted site is must be a surface-state site or a position close to particles surface. The sample synthesized with 0.006 mol/L CTAB and annealing at 600 °C has the smallest surface/volume (1/D≈0.04 nm^{-1}) indicated that Eu faction located in surface-state site is small, Large particles have a low volume/surface ratio and lead to a low density of defects, resulting in the larger fractional number of Eu^{3+} ions in substitution sites of LaF_3 matrix. The sample synthesized with 0.006 mol/L CTAB and annealing at 600 °C has the largest particles and about 95% of Eu^{3+} ions could be positioned in the high symmetric site, which engaged in the strong luminescence intensity and long lifetime.

Table 3-2 Eu fraction in high symmetric site of $LaF_3:Eu^{3+}$ nanoparticles synthesized with different CTAB concentration

CTAB concentration (mol/L)	Fraction in high symmetric site (%)	Concentration in high symmetric (mol%)
0	88.1	4.41
0.006	94.6	4.73
0.009	84.1	4.21
0.015	73.0	3.65

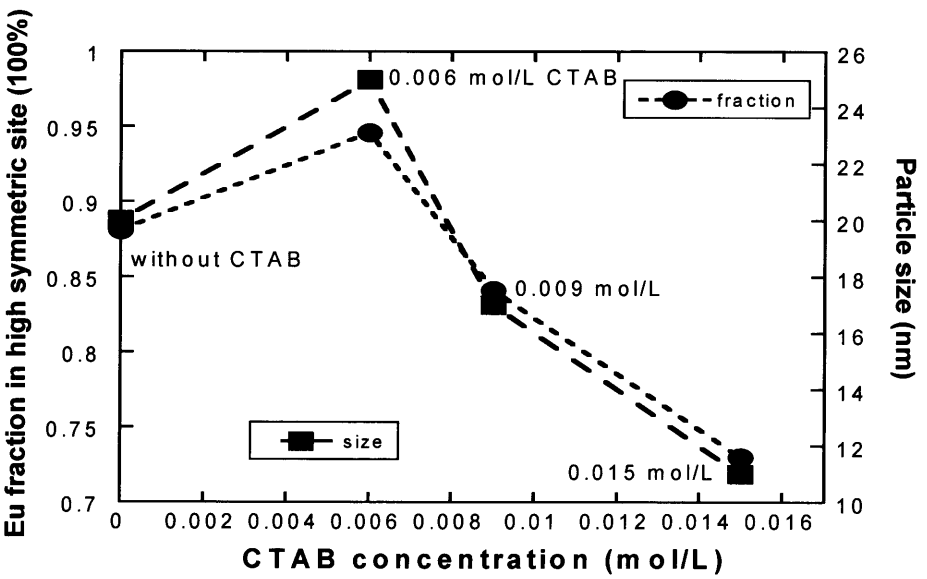

Figure 3-14 Eu fraction in high symmetric site and particle size of $LaF_3:Eu^{3+}$ nanoparticles synthesized with different CTAB concentration.

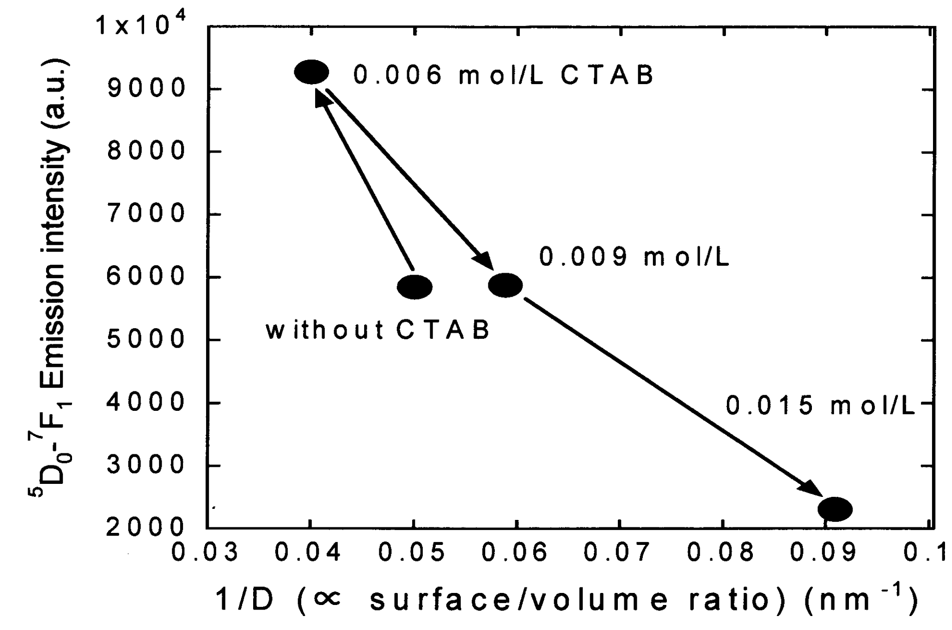

Figure 3-15 $^5D_0$-$^7F_1$ emission intensity as a function of reciprocal crystalline size (1/D), proportional to surface/volume ratio of $LaF_3:Eu^{3+}$ nanocrystals.

3.3.10 XRD Rietveld refinement result of $LaF_3:Eu^{3+}$ synthesized with different CTAB concentration

On the basis of the XRD patterns, the crystal structures of the prepared samples were refined by the Rietveld refinement using the software program RIETAN-FP (Izumi and Ikeda, 2000) [16]. For fitting, space groups of LaF_3 $P\bar{3}c1$ (No. 165) were used [17]. The fitting result of sample synthesized with 0.006 mol/L CTAB is shown in Figure 3-16. The solid line and dots are the Rietveld fitting and observed XRD patterns, respectively. The fitted lattice parameters of $LaF_3:Eu^{3+}$ samples and commercial LaF_3 and the difference between them were listed in Table 3-3. Comparing the Rietveld refinement results of commercial LaF_3 and Eu^{3+}-doped samples, the lattice parameters of Eu^{3+}-doped samples are slightly smaller than those of Eu free sample. The lattice parameters of sample synthesized with 0.006 mol/L CTAB were the smallest, and the differences from Eu free sample are the largest.

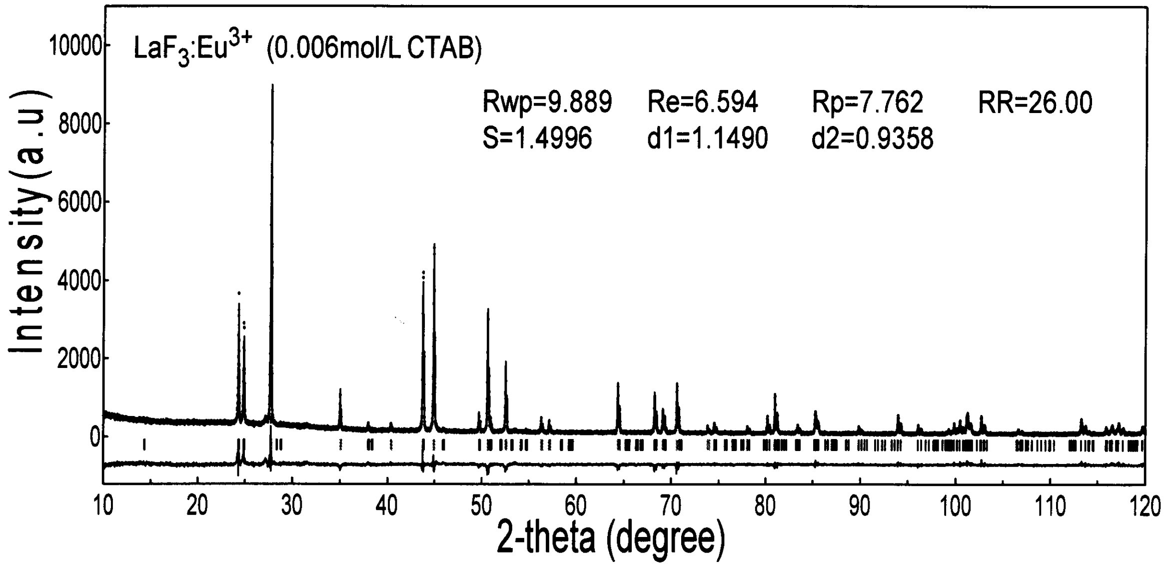

Figure 3-16 Rietveld fitting profiles for Eu free and $LaF_3:Eu^{3+}$ nanoparticles. Solid line and dots represent the calculated and measured profiles, respectively. The residual intensities are shown at the bottom of figure (jagged line), stick marks below the profile indicated the positions of the Bragg reflections.

Table 3-3 Lattice parameters of Eu free and $LaF_3:Eu^{3+}$ nanoparticles and the difference between them.

Lattice Parameter (nm)	LaF_3 :Eu^{3+} hexagonal				LaF_3 hexagonal
	CTAB Free	CTAB 0.006 mol/L	CTAB 0.009 mol/L	CTAB 0.015 mol/L	Commercial
a=*b*	0.718035 ±0.000017	0.717966 ±0.000014	0.718044 ±0.000015	0.718271 ±0.000015	0.719197 ±0.000017
Δ*a*=Δ*b* (Δ%)	0.0011 (0.15%)	0.0012 (0.17%)	0.0011 (0.15%)	0.0009 (0.13%)	
c	0.734565 ±0.000011	0.734473 ±0.000009	0.734585 ±0.000009	0.734726 ±0.000009	0.735726 ±0.000010
Δ*c* (Δ%)	0.0011 (0.1578%)	0.0012 (0.17%)	0.0011 (0.15%)	0.0009 (0.13%)	

Table 3-4 Summary of Eu concentration analysis in LaF_3: Eu^{3+} lattice matrix

Lattice Parameter (nm)	LaF_3 :Eu^{3+} hexagonal			
	CTAB Free	CTAB 0.006 mol/L	CTAB 0.009 mol/L	CTAB 0.015 mol/L
Δa=Δb	0.0011	0.0012	0.0011	0.0009
Δc	0.0012	0.0013	0.0012	0.0010
(Δa+Δc)/2	0.00115	0.00125	0.00115	0.00095
χ	0.0424	0.0461	0.0424	0.0350

Taking account of the linear relation between the lattice parameters and the lanthanide ion radius, an expected Eu ions concentration doped in LaF_3 lattice matrix can be calculated using the following function

$$\chi = \frac{\Delta(d_{LaF3} - d_{LaF3:Eu})}{\Delta(d_{LaF3} - d_{EuF3})} \qquad \text{Eq.(3-1)}$$

where $d_{LaF3:Eu}$: lattice constant of LaF_3:Eu

d_{LaF3}: lattice constant of LaF_3

d_{EuF3}: lattice constant of EuF_3 (a=b=0.692 nm, c=0.7086 nm)(JCPDS: 32-0373)

x: Eu concentration in LaF_3:Eu^{3+}.

The calculated results were listed in Table 3-4. Lattice constant of LaF_3 (a=b=0.7192 nm, c=0.7357 nm) obtained by Rietveld fitting in this study were used. The Eu concentration doped in LaF_3:Eu^{3+} lattice matrix for samples synthesized without CTAB, with 0.006 mol/L CTAB, 0.009 mol/L CTAB and 0.015mol/L CTAB are 4.24 mol%, 4.61mol%, 4.24 mol% and 3.50mol%, respectively. So the concentration of Eu ions replacing La ions in LaF_3:Eu^{3+} is the highest in the sample synthesized with 0.006 mol/L CTAB among synthesized samples, which is well consisted with the analysis result of $^5D_0$-$^7F_{1,2}$ decay curves.

3.4 Conclusion

In this chapter, size tuned $LaF_3:Eu^{3+}$ nanocrystals in hexagonal phase have been synthesized by a hydrothermal method with CTAB as a size-controlling agent. The measurements of photoluminescence and X-ray diffraction evidenced successful doping of Eu^{3+} ions in LaF_3 nanocrystals. The size plays important roles on the luminescence intensity. By XRD Rietveld refinement and the decay curve analysis, the luminescence intensity shows the same tendency as that of particle size. In large particles Eu^{3+} ions preferred to locate high symmetric site (substitution-state site), low ratio of surface/volume in large particles and low defects density inside particle induced strong luminescence intensity from doped Eu ions. When synthesized with 0.006 mol/L CTAB and heated at 600 °C $LaF_3:Eu^{3+}$ nanocrystals reached to the largest size and exhibited the strongest luminescence among synthesized samples, which could be explained by well-dispersion of Eu^{3+} ions in a higher symmetric site in a trigonal prism without Eu^{3+} clustering accompanying with concentration quenching. It was found that the 94.6 % of Eu^{3+} ions were positioned in higher symmetric sites in a trigonal prism in LaF_3 lattice and engaged in this strong photoluminescence.

3.5 References

---

1. X.T. Zhang, T. Hayakawa, M. Nogami, "Size-dependence of $LaF_3:Eu^{3+}$ nanocrystals on Eu^{3+} photoluminescence intensity", IOP Conf. Series: Materials Science and Engineering 1 (**2009**) 012021.

2. X.T. Zhang, T. Hayakawa, M. Nogami and Y, Ishikawa "Synthesis and luminescence properties of well-dispersed $LaF_3:Eu^{3+}$ nanocrystals", Journal of Ceramic Processing Research, in press.

3. X.J. Wang, S.H. Huang, R. Reeves, W. Well, M.J. Dejneka, R.S. Meltzer and W.M. Yen, "Studies of the spectroscopic properties of Pr^{3+} doped LaF_3 nanocrystals/glass" J. Lumin. **2001**, 94/95, 229-233.

4. H.R. Zheng, X.T. Wang, M.J. Dejneka, "Up-converted emission in Pr^{3+} doped fluoride nanocrystals-based oxyfluoride glass ceramics" J. Lumin. **2004**, 108, 395-399.

5. S. Tanabe, H. Hayashi, T. Hanada, N. Onodera, "Fluorescence properties of Er^{3+} ions in glass ceramics containing LaF_3 nanocrystals", Opt. Mater. **2002**, 19, 343-349.

6. M.J. Dejneka, "The luminescence and structure of novel transparent oxyfluoride glass-ceramics", J. Non-Cryst. Solids, **1998**, 239, 149-155.

7. S. Fujihara, C. Mochizuki, T. Kimura, "Formation of LaF_3 microcrystals in Sol- Gel silica", J. Non-Cryst. Solids, **1999**, 244, 267-274.

8. B.S. Zhuchkov, V.P. Tolstoy, I.V. Murin, "Synthesis of ScF_3, LaF_3 nanolayers and $n LaF_3$-$m ScF_3$ multinanolayers at the surface of silicon by successive ionic layer deposition method", Solid State Ionics, **1997,** 101-103, 165-170.

9. J.F. Zhou, Z.S. Wu, Z.J. Zhang, W.M. Liu, and H.X. Dang, "Study on an antiwear and extreme pressure additive of surface coated LaF_3 nanoparticles in liquid paraffin", Wear, **2001**, 249, 333-337.

10. D.B. Pi, F. Wang, X.P. Fan, M.Q. Wang and Y. Zhang, "Luminescence behavior of Eu^{3+} doped LaF_3 nanoparticles", Spectrochim. Acta Part A, **2005,** 61, 2455-2459.

11. J.X. Meng, M.F. Zhang, Y.L. Lin, S.Q. Man, "Molecular and bio-molecular spectroscopy" Spectrochim. Acta Part A, **2007,** 66, 81-85.

12. P. Ekwall, L. Mandell, P. Solyom, J. Coll, "The aqueous cetyltrimethylammo- nium bromide solutions", Interf. Sci. **1971**, 35, 519-528.

13. G. Porte, J. Appell, Y. Poggi, "Experimental investigations on the flexibility of elongated cetylpyridinium bromide micelles", J. Phys. Chem. **1980**, 84, 3105-3110.

14. Y. Sakaiguchi, T. Shikata, "Electron microscope study of viscoelastic cationic surfactant systems", Colloid and Polymer Science, **1987**, 265, 750-753.

15. Carnall, W. T.; Fields, P. R.; Rajnak, K. "Electronic energy levels of the trivalent lanthanide aquo ions. IV. Eu^{3+}", J. Chem. Phys. **1968**, 49, 4450-4455.

16. F. Izumi, "The Rietveld Method,"ed. by R. A. Young, Oxford University Press, Chap. 13 (1993).

17. Handbook on the Physics and Chemistry of Rare Earths; Elsevier North-Holland: Amsterdam, the Netherlands, Vol. 5, 1982.

Chapter 4. Effect of matrix GdF_3 polytype on luminescence properties of doped Eu ion

In this chapter, it is shown that $GdF_3:Eu^{3+}$ nanophosphors with hexagonal or orthorhombic structure have been succeeded to be selectively synthesized at room temperature for the first time via a simple soft chemical route. The structure and morphology of $GdF_3:Eu^{3+}$ nanophosphors were controlled by using different fluoride precursors. Hexagonal $GdF_3:Eu^{3+}$ nanocrystals were formed when $NaBF_4$ was used as a fluoride precursor, while orthorhombic $GdF_3:Eu^{3+}$ nanocrystals were obtained with NaF or NH_4F fluoride precursor. It was also experimentally revealed that hexagonal $GdF_3:Eu^{3+}$ nanophosphors emitted essentially stronger Eu^{3+} luminescence than orthorhombic ones. The formation mechanism of GdF_3 nanocrystals and how the polytype structure influenced the luminescence properties were discussed[1,2].

4.1 Introduction

The lanthanide fluoride compounds LnF_3 and $ALnF_4$ (A = alkali metal, Ln = rare- earth element) have been widely used in many fields, such as optical telecommunication, lasers, new optoelectronic devices, diagnostics, and biological labels [3,4,5,6,7]. The polytype engineering of these materials has recently attracted attention. In fact, polytype $NaYF_4$ (or $NaGdF_4$) with hexagonal and cubic structures have been well documented [8,9,10,11,12]. However, studies of polytype LnF_3, including GdF_3, with hexagonal and orthorhombic structures are very few, most of which were focused on the phase transition mechanism at high temperatures [13,14,15,16,17]. Recently, stronger luminescence from Eu^{3+} in hexagonal EuF_3 than in orthorhombic EuF_3 has been reported [18]. This suggests that the polytype control of matrix LnF_3 makes it possible to increase the light-emitting probability of rare-earth-doped LnF_3 by the changing of atomic coordination around the doped rare earth.

4.2 Experiment of polytype $GdF_3:Eu^{3+}$

All reagents were obtained from Aldrich Chem. Co. and used as received without further purification. Typical procedures for the synthesis of $GdF_3:Eu^{3+}$ nanocrystals are described as follows (see in Figure 4-1). First, 0.005 mol of $Gd(NO_3)_3 \cdot 6H_2O$ and 0.00025 mol of $EuCl_3 \cdot 6H_2O$ were dissolved in 100 ml of deionized water in a beaker at room temperature. After mechanical stirring for about 20 min, an aqueous solution of 0.015 mol of $NaBF_4$ (sample A), 0.015 mol of NH_4F (sample B) and 0.015 mol of NaF (for sample C) was added dropwise. After constant stirring for 12 h at room temperature, a white precipitate was formed. Each precipitate was collected by three cycles of centrifugation and successive washing with water and ethanol. Subsequently, the final product was dried in an oven at 80 °C. The nominal Eu^{3+} concentration was fixed at 5 mol%. To study the change in the lattice parameter upon adding Eu^{3+} to GdF_3, Eu-free GdF_3 polytype samples were also prepared by the same method. The Eu-free samples A and B are denoted as A° and B°, respectively.

XRD analysis was performed on a Philips X`pert system using Cu K_{α} radiation at a 45 kV voltage and a 40 mA current. The morphology, size and Eu^{3+} concentration of the products were examined by a scanning electron microscopy of HITACHI S-4500 microscope equipped with EDX (EMAX-7000). The structural characteristics of the samples were further examined with a transmission electron microscope (JEOL, JEM-4000FX) using an accelerating voltage of 400 kV. The excitation and PL spectra were obtained using a F-7000 fluorescence spectrophotometer (Hitachi Co.). The PL decay curves of $^5D_0 \rightarrow {}^7F_{1,2}$ transitions were recorded using a time-resolved fluorescence system (Oriel Instruments: InstaSpec™ V) under excitation with a 337.1 nm N_2 laser (Usho, KEC-200).

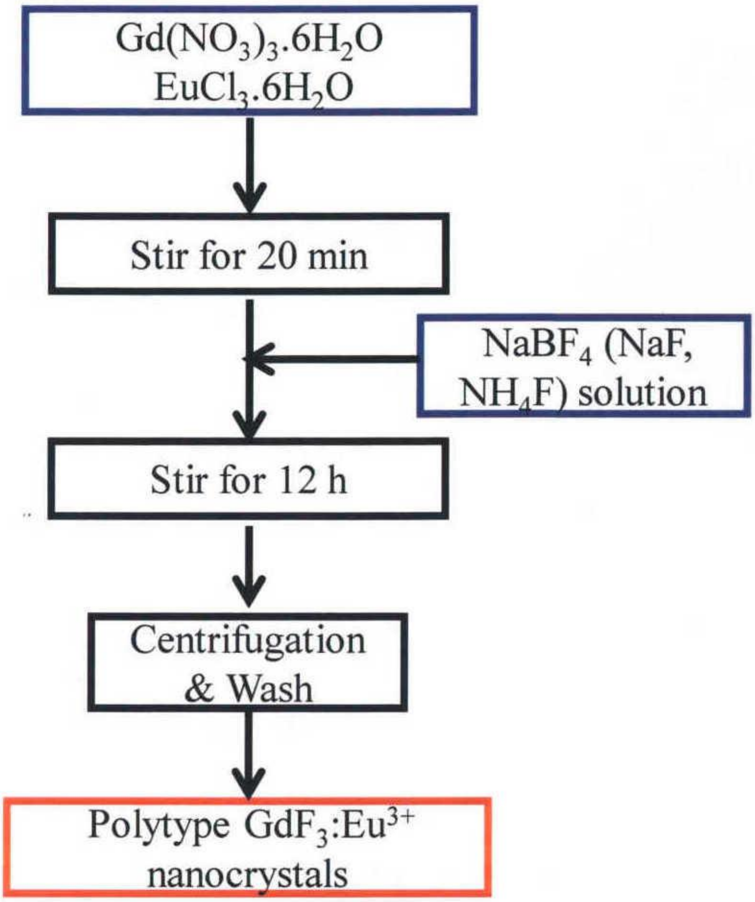

Figure 4-1 The flow chart of preparation of polytype $GdF_3:Eu^{3+}$ nanoparticles.

4.3 Results and discussion

4.3.1 XRD pattern of Polytype $GdF_3:Eu^{3+}$ nanoparticles

Figure 4-2 shows the X-ray powder diffraction patterns of samples A, B and C. The XRD pattern of sample B is similar to that of sample C, these two patterns can be readily identified orthorhombic GdF_3 (PDF No.12-0788). It can be found that a (020) peak of sample B is sharper than that of sample C so that sample B seems to have better crystalinity. On the other hand, the XRD pattern of sample A clearly differs from those of B and C. Since the XRD data for the hexagonal GdF_3 have not been reported, this phase is compared with hexagonal SmF_3 (PDF No. 05-0563) and all the diffraction peaks in Figure 4-2 (A) can be indexed to the hexagonal structure.

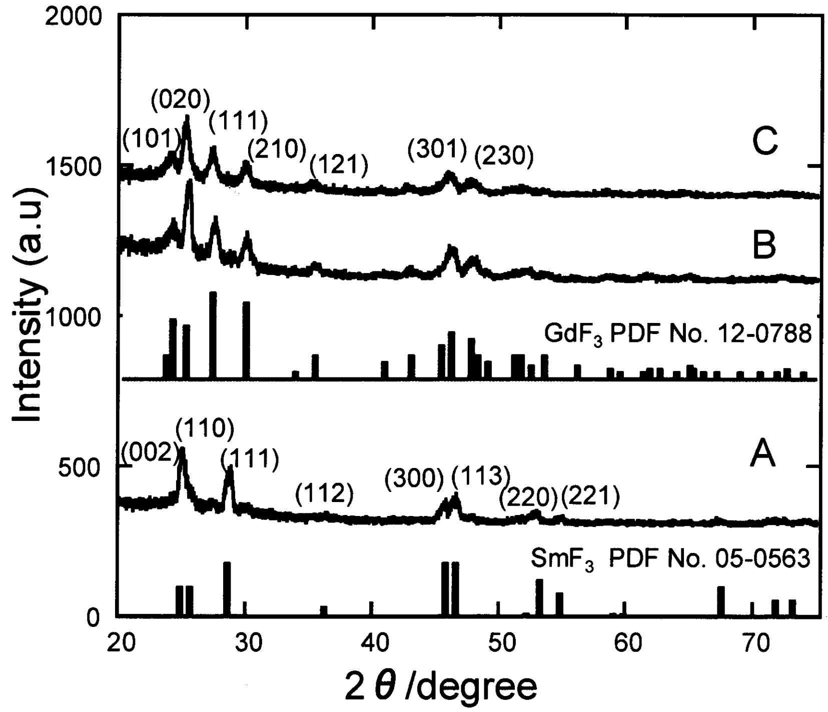

Figure 4-2 XRD patterns of the sample A, B and C synthesized with $NaBF_4$, NH_4F and NaF, respectively.

4.3.2 SEM and TEM images of polytype GdF_3:Eu^{3+} particles

Figure 4-3 shows SEM, TEM images and Selected Area Electron Diffraction (SAED) pattern of sample A. SEM image (a) shows that the particles have "*disc*"-like morphology with size about 0.9-1.5 μm in diameter. TEM image (b) elucidates the unique morphology same as SEM image. From the magnified TEM image (inset), it can be seen that this round shape is brought by aggregate of "*plate*"-like clusters. The SAED pattern (c) indicates that there are two kinds of clusters in *disc*-like particles. The lattice constant of one kind of clusters was $a=b$ =0.5926 nm, and that of the other kind of clusters was $a=b$=0.6928 nm. It should be noted in spite of the difference of lattice constant, both clusters were hexagonal and each other kept epitaxial relationship.

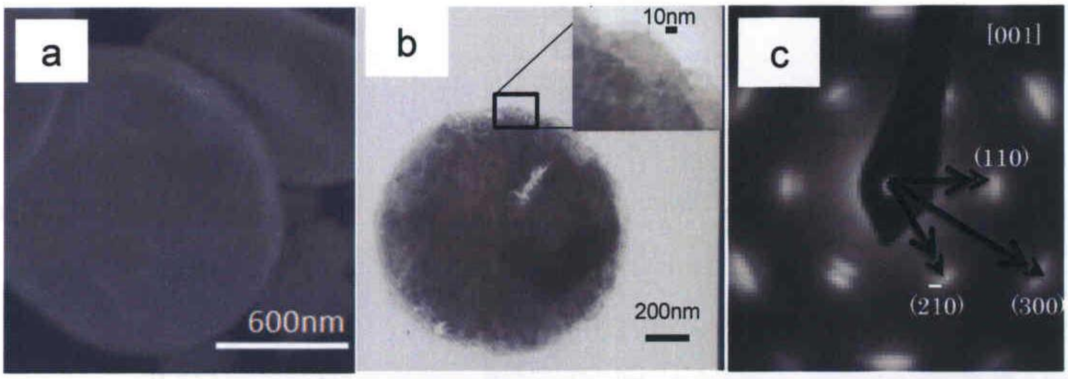

Figure 4-3 SEM image (a), TEM image (b) and SAED pattern (c) of sample A (Inset shows the magnified TEM image (b)

Images of SEM and TEM of sample B and C are obtained and shown in Figure 4-4. For sample B, SEM image (a) and TEM image (b) shows that the particles exhibited a round shape with a hole in it and the particle size was about 0.8-1.2 μm in diameter, estimated from the magnified TEM image (inset b). It can be clearly seen that this round shape is formed due to clustered "*hair*"-like nanoparticles. The SEM image (c) and TEM image (d) of sample C shows "*spindle*"-like morphology with dimensions of 300-400 nm in length and 60-100 nm in width. SAED pattern of sample C is shown in Figure 4-5, which indicates that spindle-like clusters were orthorhombic and almost aligned like a single crystal, but it contained slightly tilted ones toward [011].

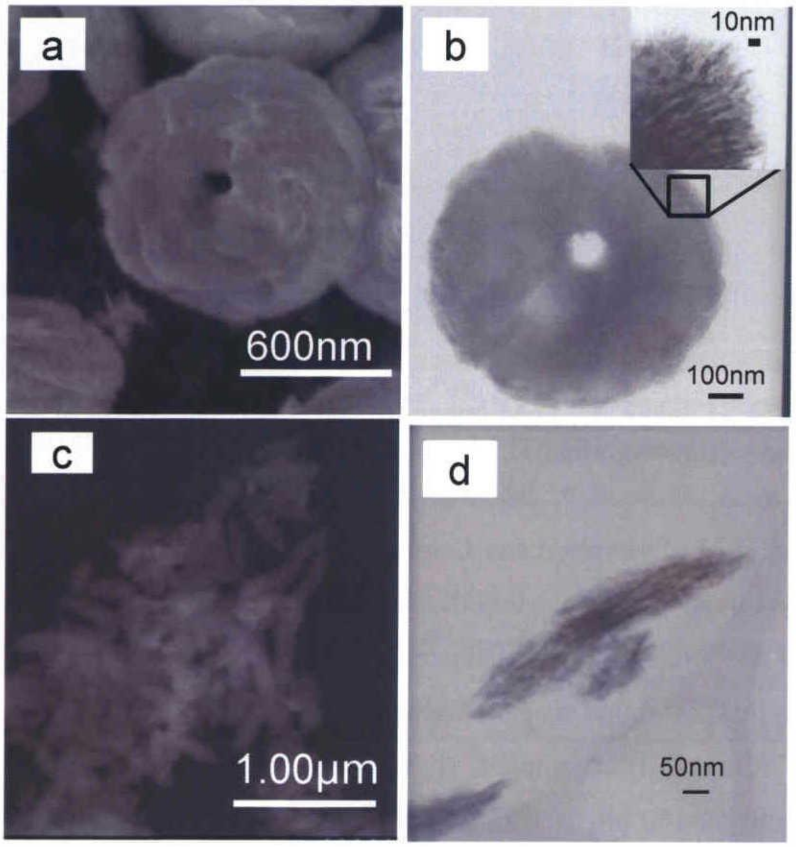

Figure 4-4 SEM image (a), TEM image (b) and SAED pattern (c) of sample B (Inset shows the magnified TEM image (b). TEM image of smaple C (d).

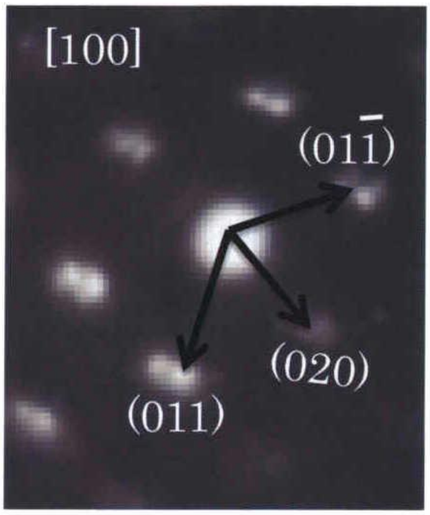

Figure 4-5 SAED pattern of sample C with orthorhombic structure.

4.3.3 Fluorite precursors effect on GdF_3 polytype structure

Crystal structure and morphology of $GdF_3:Eu^{3+}$ nanoparticles depended on the fluoride source, even though the synthetic conditions were identical except for the fluoride sources. Recent investigations also demonstrated the formation of hexagonal and orthorhombic GdF_3 nanocrystals, and however these nanocrystals were synthesized at higher temperatures (>300 °C)[19, 20, 21, 22]. Our method is very simple and employed at room temperature, where it is demonstrated that different fluoride sources have the strong impacts not only on morphologies but also on crystal structures of GdF_3 nanocrystals.

Here, we emphasized the crucial effect of $NaBF_4$ on the crystalline phases of the products in our current synthesis. In the case of NH_4F and NaF, a white precipitate appeared immediately after the gadolinium nitrate solution was mixed with sodium or ammonium fluoride, which indicated that the nucleation had taken place rapidly. On the other hand, the initial solution was kept clear and transparent when $NaBF_4$ was added as a fluoride source, suggesting that no fluoride precipitation was formed. The white precipitate was formed after stirring for 20 min. The probable reaction processes for the formation of GdF_3 can be summarized as follows:

$$BF_4^- + 3H_2O \leftrightarrow 3HF + F^- + H_3BO_3 \qquad \text{Eq.(4-1)}$$

$$2H_3BO_3 + 2Na^+ \rightarrow Na_2B_2O_4 + 2H_2O + 2H^+ \qquad \text{Eq.(4-2)}$$

$$Gd^{3+} + 3F^- \rightarrow GdF_3 \qquad \text{Eq.(4-3)}$$

In an aqueous solution, $NaBF_4$ was slowly hydrolyzed to produce BO_3^{3-} and F^- anions, as shown in Eq.(4-1) as the equilibrium constant of the hydrolysis reaction was very small ($K_\theta = 6.41 \times 10^{-12}$ at 25 °C) [23], the concentration of F^- anions in the reaction solution was kept at a low level [24, 25], from the view of the reaction equilibrium, and so the low F^- concentration is brought in an acidic environment. Furthermore, the composition analysis of the clear solution after centrifugation demonstrated the formation of H_3BO_3 and $Na_2B_2O_4$ (Eq.(4-2)). The pH value of the aqueous solution was approximately equal to 6.0 at the beginning of the reaction, and when the reaction was complete the pH value decreased to 1.5. Finally, Gd^{3+} ions were reacted with F^- anions produced during the slow hydrolysis of $NaBF_4$, so as to form GdF_3 nuclei, as presented in Eq.(4-3). Because of the very low production rate of F^- anions in solution, the particle growth of the precipitated GdF_3 solid was very slow. Additionally, the hexagonal-structure could be stabilized if the fluorine anions were deficient [26], so the deficiency of F^- anions due to the low F^- concentration in solution might help synthesize hexagonal structure.

4.3.4 PLE spectra of polytype $GdF_3:Eu^{3+}$

PLE spectra of 592 nm light emission from polytype $GdF_3:Eu^{3+}$ samples are shown in Figure 4-6. The excitation spectra of the $^5D_0$ red emission indicate that the sharp peak located at 274 nm corresponds to excitation into $^6I_{J'}$ (J'=7/2-17/2) ($^8S_{7/2}\rightarrow{}^6I_{J'}$) levels of Gd^{3+}, and the peak located at 396nm corresponds to the $^7F_0\rightarrow{}^5L_6$ direct excitation of Eu^{3+}. The short wavelength excitation confirms the occurrence of energy transfers from $^6I_{J'}$ (J'=7/2-17/2) level of Gd^{3+} to Eu^{3+}. The 4*f* energy level overlap between the ^6P_J states of Gd^{3+} and the ^5H_J states of Eu^{3+} allows energy transfer from Gd^{3+} to Eu^{3+} and thus energy transfer route from Gd^{3+} to Eu^{3+} can be explained [27] as follows: Gd^{3+} ions are first excited to $^6I_{J'}$ (J'=7/2-17/2) energy level and through nonradiative relaxation decay to ^6P_J states, and then from this level transfer its excitation energy to Eu^{3+} ion, resulting in the emission of visible photons due to the Eu^{3+} : $^5D_0$ - ^7F_J transition.

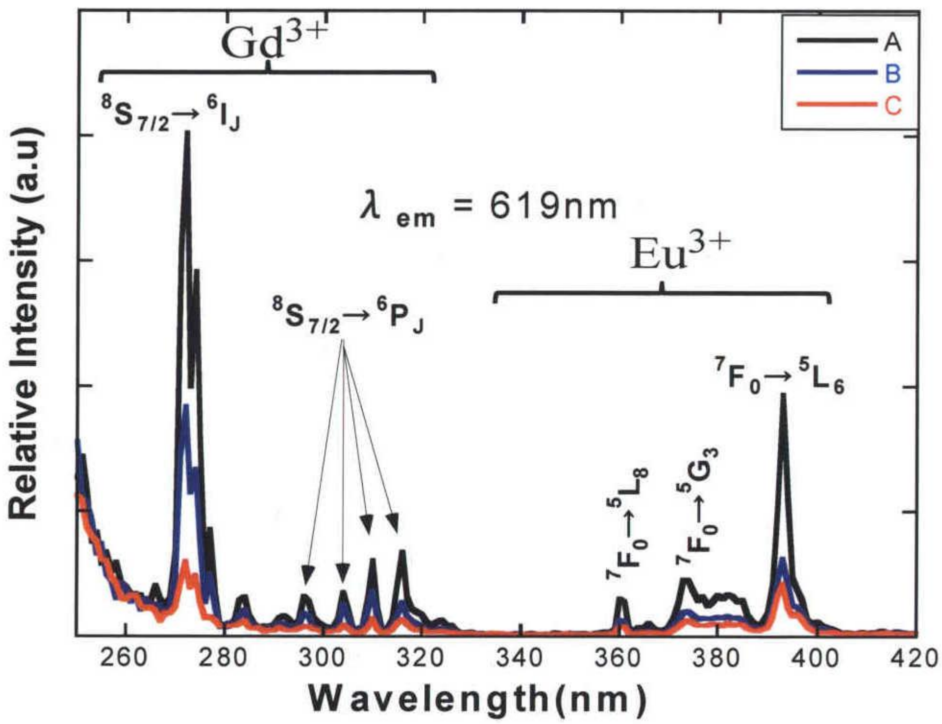

Figure 4-6 Photoluminescence excitation spectra of the Eu^{3+} doped in polytype GdF_3 nanocrystals ((A) hexagonal, (B) and (C) orthorhombic).

4.3.5 PL spectra of polytype $GdF_3:Eu^{3+}$

Room-temperature PL spectra of sample A, B and C excited at 274 nm and the spectra of sample A (hexagonal) and sample B (orthorhombic) excited at 396 nm and 274 nm are presented in Figure 4-7 and Figure 4-8, respectively. The luminescence bands are assigned according to Carnalls' paper [28]. In both emission spectra has shown two intense bands associated with $^5D_0 \rightarrow {}^7F_1$ and $^5D_0 \rightarrow {}^7F_2$ transitions for Eu^{3+}. The peak centered at 592 nm corresponds to the $^5D_0 \rightarrow {}^7F_1$ magnetic dipole transition, and the peak centered at 619 nm corresponds to the $^5D_0 \rightarrow {}^7F_2$ electric dipole transition. The little peaks located at 525 nm, 530 nm and 554 nm were corresponding to the $^5D_1 \rightarrow {}^7F_J$ transitions [15]. The intensity of the 592 nm PL from hexagonal sample A was much larger than that of orthorhombic samples of B and C. As the excitation of 274 nm corresponds to the transition $^8S_{7/2} \rightarrow {}^6I_J$ of Gd^{3+}, and 396 nm excitation corresponds to the transition $^7F_0 \rightarrow {}^5L_6$ of Eu^{3+} ions (see in Figure 4-8), it can be concluded that both the energy transfer from Gd^{3+} to Eu^{3+} and the intratransition in Eu^{3+} can excite PL (592 nm and 619 nm). Hexagonal $GdF_3:Eu^{3+}$ emitted a stronger luminescence than orthorhombic $GdF_3:Eu^{3+}$ under both excitation wavelengths. More remarkably, the luminescence intensity of the nanocrystals excited at 274 nm is in both cases stronger than that of the nanocrystals excited at 396 nm. The intensity ratio of the 592 nm emission peaks under different excitation at 274 nm and 396 nm was estimated to be 5.5 for the hexagonal structure. Similarly, the ratio of the 592 nm emission intensity at 274 nm and 396 nm excitation was estimated to be 2.6 for the orthorhombic structure. Therefore, the energy transfer probability from the Gd^{3+} ion to the Eu^{3+} ion in the hexagonal structure is higher than that in the orthorhombic structure if we assume that the absorption cross sections of the transition $^7F_0 \rightarrow {}^5L_6$ in Eu^{3+} ions are the same.

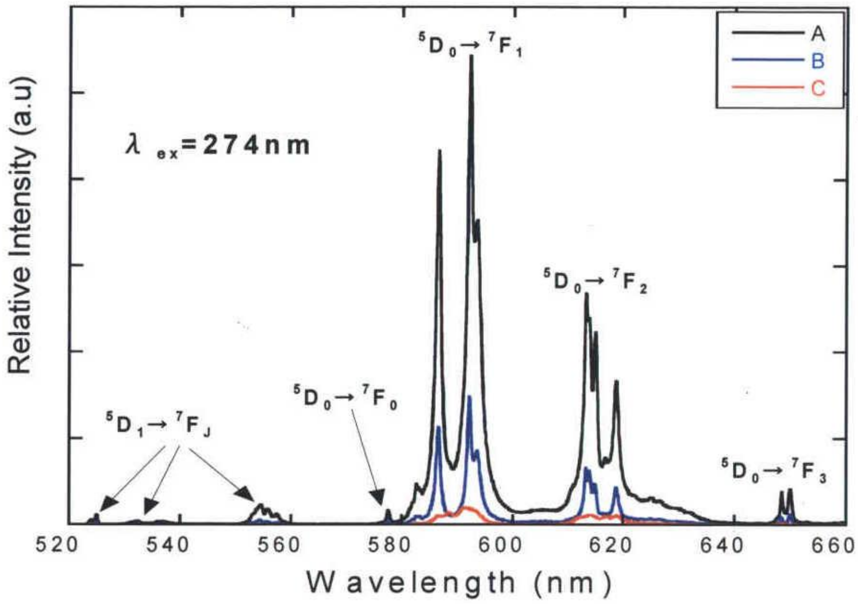

Figure 4-7 Photoluminescence spectra of Eu^{3+} ions doped in polytype GdF_3 nanocrystals ((A) hexagonal, (B) and (C) orthorhombic).

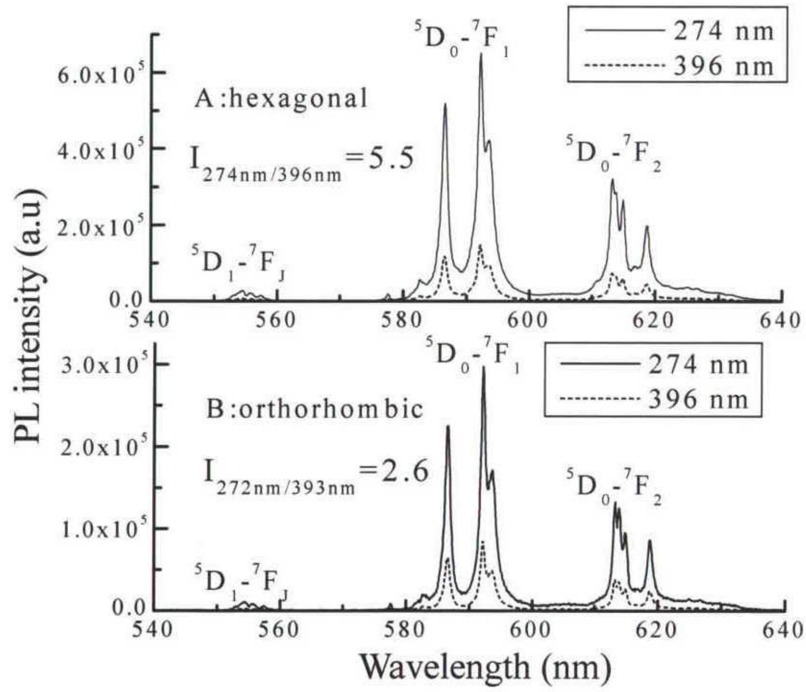

Figure 4-8 Emission spectra of hexagonal (upper) and orthorhombic (lower) $GdF_3:Eu^{3+}$ nanophosphors excited at 274 nm and 396 nm.

4.3.6 Eu concentration analysis by EDX spectra

EDX spectra of the samples studied were shown in Figure 4-9. Peaks located at about 5.845 keV and 6.056 keV were assigned to the Eu $L_{\alpha 1}$ and Gd $L_{\alpha 1}$, respectively. The spectra indicated that Eu concentrations in $GdF_3:Eu^{3+}$ were independent on the fluoride sources and a bit decreased from the nominal value (5 mol%) to 4.2-4.4 mol%. In was found that the obtained $GdF_3:Eu^{3+}$ nanophosphors had the almost same Eu^{3+} concentration. Therefore it can be concluded that the stronger PL intensity of hexagonal sample A than these of orthorhombic sample B and C would be caused by the polytype host GdF_3. In EDX spectra (not shown here), no peaks from Na and N elements can be found so that Na and N elements concentration in particles are too low to be detected. Thus, $NaGdF_4$ and NH_4GdF_4 have not be produced during the synthesis, and even if they exist, they are so little and can be ignored. It can also be found that hexagonal GdF_3 nanocrystals have higher O-to-Gd (O/Gd) elemental ratio than orthorhombic GdF_3 nanocrystals does. As a result, O concentration is higher in hexagonal crystals than in orthorhombic crystals. So, although hexagonal $GdF_3:Eu^{3+}$ nanocrystals have relatively higher amount of impurities related with OH groups, they exhibited stronger luminescence intensity than orthorhombic $GdF_3:Eu^{3+}$ nanocrytals.

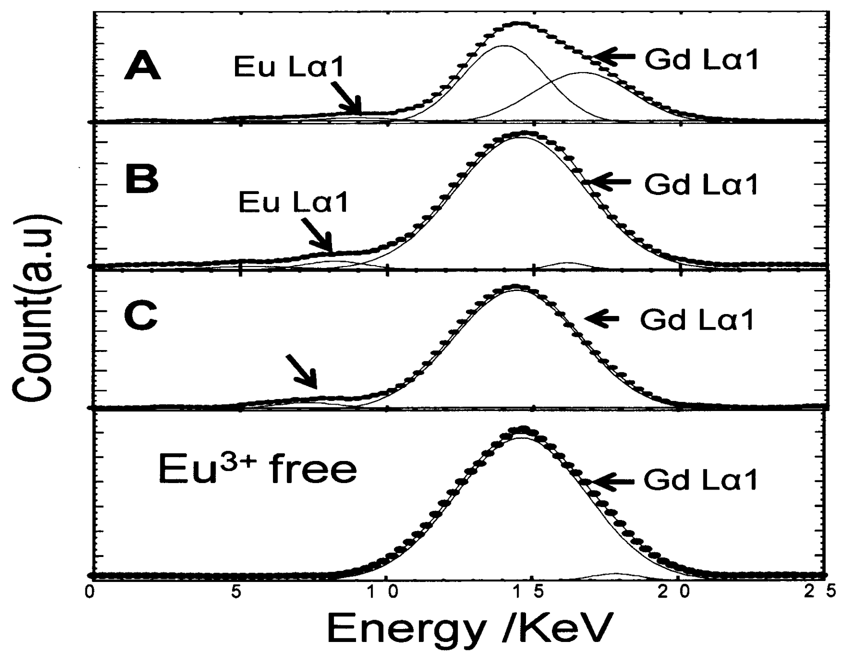

Figure 4-9 EDX spectra of different samples (A, B and without Eu^{3+})

4.3.7 XRD Rietveld refinement result of polytype $GdF_3:Eu^{3+}$

In order to study the polytype $GdF_3:Eu^{3+}$ nanoparticles structure with Rietveld refinement method, fine XRD patterns of sample A (hexagonal) and B (orthorhombic) as well as the non-doped Eu samples A^o and B^o (prepared with the method with sample A and B, respectively) were detected and shown in Figure 4-10. On the basis of the XRD patterns, the crystal structures of the prepared samples were refined by the Rietveld refinement using the software program RIETAN-FP (Izumi and Ikeda, 2000) [29]. For fitting, space groups of LnF_3 Pnma (D162h, No. 62) and P$\overline{3}$C1 (D43d, No. 165) [30] were used for samples A (A^o) and B (B^o), respectively.

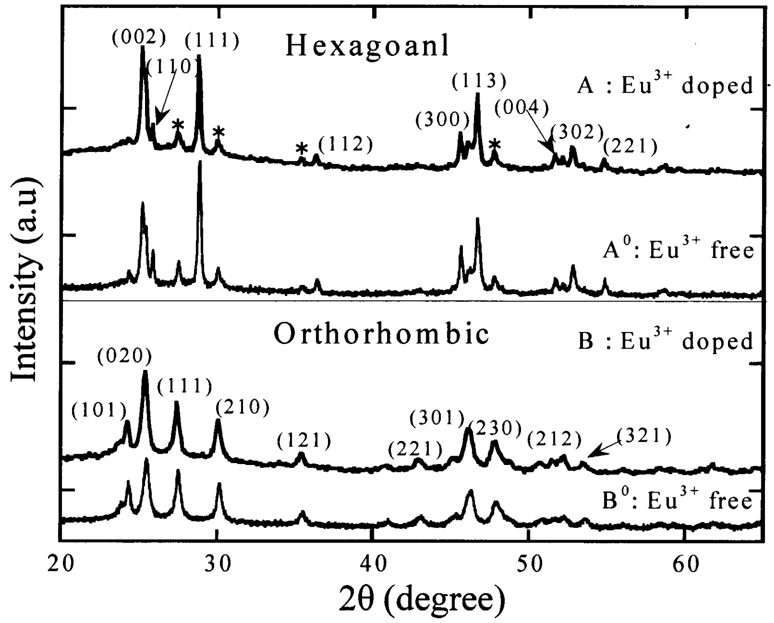

Figure 4-10 XRD patterns of hexagonal (upper panel) and orthorhombic (lower panel) GdF_3 nanophosphors. Upper and lower patterns in the panels are Eu doped and Eu free, respectively.

In Table 4-1, the reported and fitted lattice parameters of LnF_3 materials are listed. The lattice parameters of LnF_3 linearly decreased in the sequence of SmF_3, EuF_3, GdF_3, and TbF_3, depending on the rare-earth ion radius in the orthorhombic structure. The lattice parameters *a*, *b*, and *c* of orthorhombic GdF_3 in this work (a=0.6563 nm, b=0.6971 nm, and c=0.4387 nm) were slightly smaller than the reported data (a=0.6571 nm, b=0.6984 nm, and c=0.439 nm). Only the lattice parameters of hexagonal SmF_3 and EuF_3 are listed in Table 4-1, owing to the lack of data for hexagonal GdF_3 and

TbF_3 in the JCPDS (Joint Committee for Powder Diffraction Standards) database. In hexagonal LnF_3, a linear decrease in the lattice parameters with the rare-earth ion radius was also confirmed. The fitting results of samples A and B are shown in Figure 4-11. The solid line and dots are the Rietveld fitting and observed XRD patterns, respectively. Comparing the Rietveld refinement results of Eu^{3+}-free and Eu^{3+} -doped samples, the lattice parameters of both Eu^{3+}-doped hexagonal and orthorhombic samples are slightly larger than those of the Eu^{3+}-free samples. As the valence and radius of the Gd ion were similar to those of the Eu ion, the replacement of Gd ion by the Eu ion doped into GdF_3 is reasonable. Taking account of the linear relation between the lattice parameters and the lanthanide ion radius, an expected increase in the lattice parameters can be calculated using

$$d_{GdF3:Eu} = d_{GdF3} + (d_{GdF3} - d_{EuF3}) \times \chi, \qquad \text{Eq.(4-5)}$$

$d_{GdF3:Eu}$: lattice constant of GdF_3:Eu

d_{GdF3}: lattice constant of GdF_3

d_{EuF3}: lattice constant of EuF_3

x: Eu concentration in GdF_3:Eu.

In the case of 4% Eu doping, the increases in lattice parameters were Δa_h=0.17 pm and Δc_h= 0.10 pm in hexagonal GdF_3, and Δa_o=0.23 pm, Δb_o=0.18 pm and Δc_o=0.03 pm in orthorhombic GdF_3.

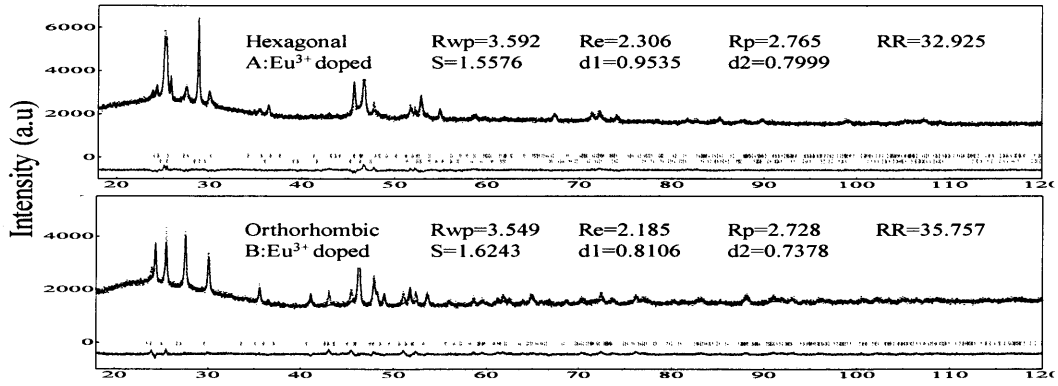

Figure 4-11 Rietveld fitting profiles for polytypes of GdF_3 (sample A and B). Solid line and dots represent the calculated and measured profiles, respectively. The residual intensities are shown at the bottom of figure (jagged line), stick marks below the profile indicated the positions of the Bragg reflections.

Table 4-1 Lattice parameters of LnF_3

Lattice Parameter (nm)	Hexagonal SmF_3 (*P63/mcm*) (12-0792*)	EuF_3 (*P$\bar{3}$c1*) (32-0373*)	GdF_3 (*P$\bar{3}$c1*) (this work A°)	$GdF_3:Eu^{3+}$ (*P$\bar{3}$c1*) (this work A)		
a=*b*	0.6952	0.6920	0.687823 ±0.000014	0.687979 ±0.000022		
c	0.7122	0.7086	0.706216 ±0.000025	0.706396 ±0.000023		
Lattice Parameter (nm)	**Orthorhombic** SmF_3 (*Pnma*) (32-0981*)	EuF_3 (*Pnma*) (33-0524*)	GdF_3 (*Pnma*) (49-1804*)	GdF_3 (*Pnma*) (this work B°)	$GdF_3:Eu^{3+}$ (*Pnma*) (this work B)	TbF_3 (*Pnma*) (37-1487*)
a	0.6672	0.6620	0.6571	0.656308 ±0.000016	0.656534 ±0.000017	0.6508
b	0.7058	0.7015	0.684	0.697124 ±0.000018	0.697388 ±0.000028	0.6948
c	0.4404	0.4396	0.439	0.438739 ±0.000011	0.439295 ±0.000014	0.4391

*JCPDS number

The measured values indicated that the increases in the lattice parameters upon 4% Eu doping in hexagonal GdF_3 were approximately Δa_h=0.16 pm and Δc_h=0.18 pm; and those in orthorhombic GdF_3 were approximately Δa_o=0.23 pm, Δb_o=0.26 pm and Δc_o=0.56 pm. The good consistency of the calculated increases in the lattice parameters with the measured values indicates that most Eu ions in GdF_3 can substitutionally be positioned at the Gd site.

On the basis of the Reitveld refinement results, crystal structures were drawn using VEST software and are shown in Figure 4-12. In both the hexagonal and orthorhombic structures, the numbers of Gd^{3+} ions around the center Gd^{3+} ion are the same but the distances between Gd^{3+} ions are different as listed in Table 4-2. In the hexagonal structure, there are four equivalent nearest-neighbor Gd ion sites from the center Gd ion and the distance was calculated to be 0.38553 nm. On the other hand, there are two equivalent nearest-neighbor Gd ion sites from the center Gd site in the orthorhombic structure and the distance was 0.39307 nm. According to the Förster resonance energy transfer theory, the energy transfer probability P_{AB} is expressed as follows [31,32]:

$$P_{AB} = 1.4 \times 10^{24} f_A f_B S/[\Delta E^2 R^6] \qquad \text{Eq.(4-6)}$$

f_A, f_B: oscillator strengths of the donor and acceptor, respectively,

S: overlap of donor emission and acceptor absorption,

ΔE: transition energy,

R: distance between the donor and acceptor.

The probability of energy transfer depends inversely on the sixth power of the distance between the donor and the acceptor. Therefore, the shorter distance between Gd^{3+} and substituted Eu^{3+} ions in the hexagonal structure can induce a higher energy transfer probability from Gd^{3+} ions to Eu^{3+} ions than that in the orthorhombic structure.

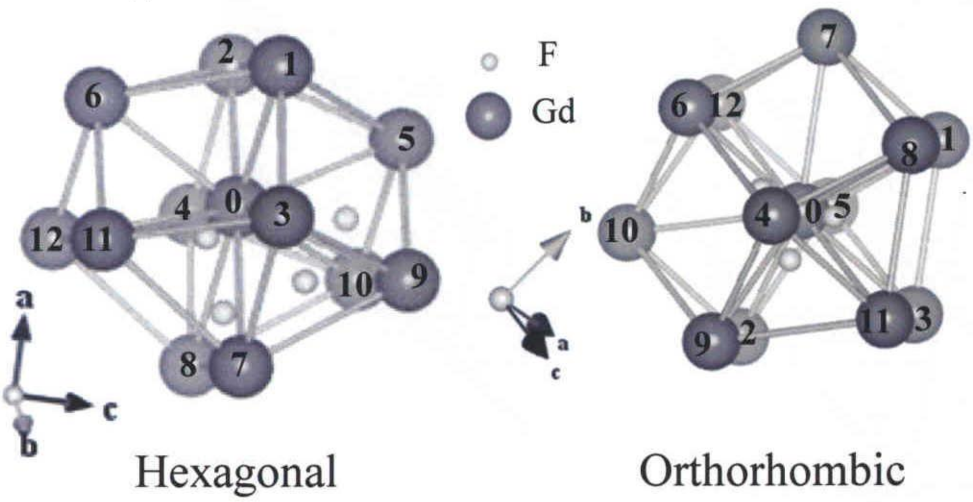

Figure 4-12 Configuration of Gd^{3+} ions in hexagonal and orthorhombic $GdF_3:Eu^{3+}$ structure according the Rietveld refinement results.

Table 4-2 $Gd_x \rightarrow Gd_0$ distance in polytype $GdF_3:Eu^{3+}$. X denotes the ion site in Figure 4-12.

x	Hexagonal Interatomic distance $Gd_x \rightarrow Gd_0$(nm)	Orthorhombic Interatomic distance $Gd_x \rightarrow Gd_0$(nm)
1	0.385532	0.393070
2	0.385532	0.393070
3	0.385532	0.394006
4	0.385532	0.394006
5	0.406382	0.394006
6	0.406382	0.394006
7	0.421907	0.437152
8	0.421907	0.437152
9	0.429091	0.437152
10	0.429091	0.437152
11	0.429091	0.439695
12	0.429091	0.439695
Average	0.40959	0.41585

4.3.8 Decay curves analysis of polytype $GdF_3:Eu^{3+}$

Figure 4-13 shows the decay curves of $^5D_0 \rightarrow {}^7F_{1,2}$ emissions for polytype $GdF_3:Eu^{3+}$ nanophosphors. Luminescence decay curves can be well fitted with a double-exponential function using the least-squares fitting method:

$$I(t)/I_0 = \alpha \exp(-t/\tau_f) + \beta \exp(-t/\tau_s), \qquad \text{Eq.(4-7)}$$

where τ_f is the decay time of the fast component, τ_s is the decay time of the slow component, and α and β are the amplitude ratios of the fast and slow components, respectively ($\alpha + \beta = 1$). The results fitted to the decay curves are summarized in Table 4-3 and Table 4-4 for hexagonal and orthorhombic $GdF_3:Eu^{3+}$, respectively. For clarity, the average lifetimes of $^5D_0 \rightarrow {}^7F_{1,2}$ emissions were also calculated with Eq.(4-7) using the fitted results and are given in Table 4-5.

$$\tau = \frac{\alpha\tau_f^2 + \beta\tau_s^2}{\alpha\tau_f + \beta\tau_s} \qquad \text{Eq.(4-8)}$$

It is very clear that hexagonal $GdF_3:Eu^{3+}$ exhibits a longer lifetime than orthorhombic $GdF_3:Eu^{3+}$, supporting the notion that Eu^{3+} ions are positioned in hexagonal systems with a higher symmetric structure.

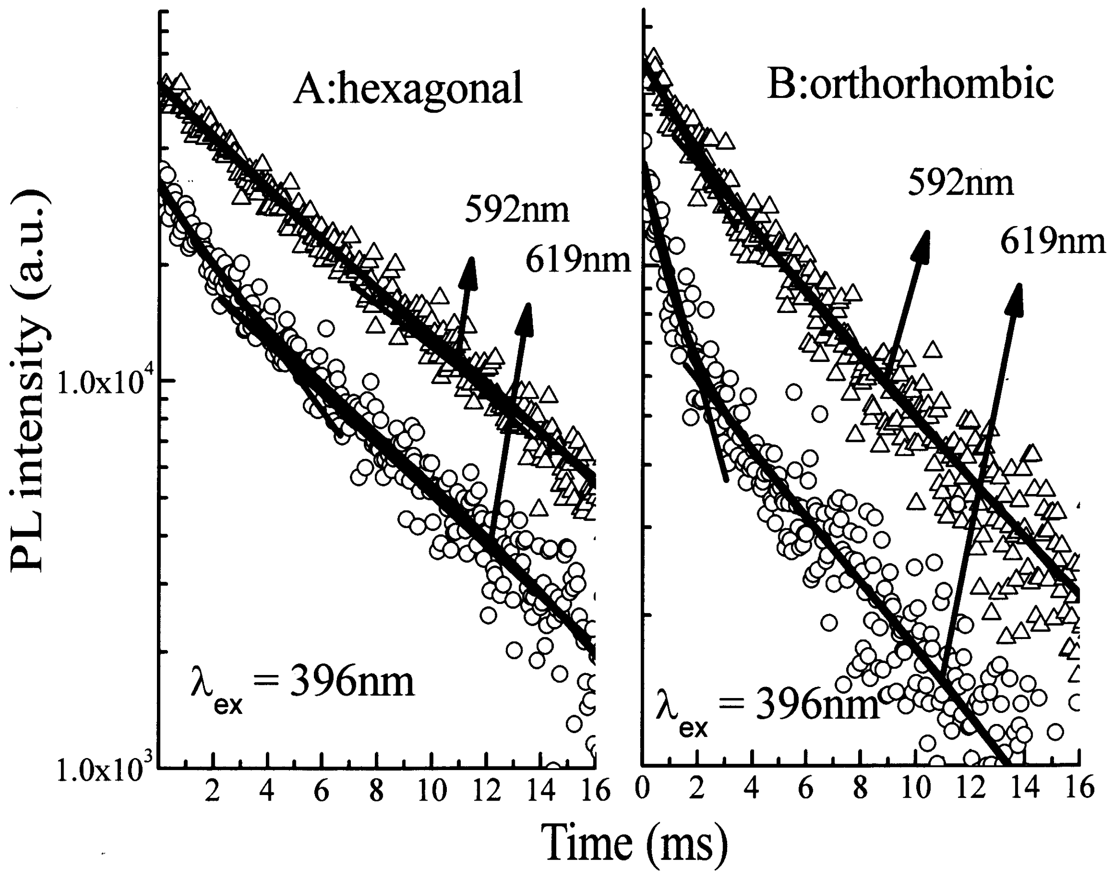

Figure 4-13 Decay curves of $^5D_0 \rightarrow {}^7F_{1,2}$ emissions (592 and 619nm) are shown by open triangles and open circles, respectively. The solid curves are fitting result to two exponential functions by a least-square fitting method. Right and left panels indicate hexagonal and orthorhombic $GdF_3:Eu^{3+}$ nanophosphors, respectively.

Table 4-3 Lifetimes and amplitude ratio obtained by fitting the decay curves of $^5D_0 \rightarrow {}^7F_1$ and $^5D_0 \rightarrow {}^7F_2$ emission for hexagonal $GdF_3:Eu^{3+}$ nanocrystals.

	$^5D_0$-$^7F_1$ emission		$^5D_0$-$^7F_2$ emission	
	fast decay	slow decay	fast decay	slow decay
Decay time / ms	4.6	14.97	1.84	8.29
Amplitude, α, β	0.57	0.43	0.36	0.64
Luminescence Intensity	2.62	6.45	0.66	5.3
Relative Contribution	29%	71 %	11%	89%
Intensity Ratio	0.29 $(=\eta_f)$	0.71 $(=\eta_s)$	0.06 $(=\xi_f)$	0.47 $(=\xi_s)$
	1.00 $(=\eta_f+\eta_s)$		0.59 *1) $(=\xi_f+\xi_s)$	
Microscopic Λ			$\Lambda_{fast} = 0.75$ *2)	$\Lambda_{slow} = 0.21$*3)
$W_{0\text{-}2}$			$W_{0\text{-}2}{}^{dis} = 0.75W_{0\text{-}1}$	$W_{0\text{-}2}{}^{hs} = 0.21W_{0\text{-}1}$

*1) corresponding to the apparent asymmetric ratio Λ of 0.59 obtained from the luminescence spectrum in Figure 4-7.
*2) $\Lambda_{fast} = \xi_f / \eta_f$,
*3) $\Lambda_{slow} = \xi_s / \eta_s$

Table 4-4 Lifetimes and amplitude ratio obtained by fitting the decay curves of $^5D_0 \rightarrow {}^7F_1$ and $^5D_0 \rightarrow {}^7F_2$ emission for orthorhombic $GdF_3:Eu^{3+}$ nanocrystals.

	$^5D_0$-$^7F_1$ emission		$^5D_0$-$^7F_2$ emission	
	fast decay	slow decay	fast decay	slow decay
Decay time / ms	1.28	7.06	0.59	5.2
Amplitude, α, β	0.25	0.75	0.4	0.6
Luminescence Intensity	0.32	5.3	0.24	3.12
Relative Contribution	5.7%	94.3 %	0.7%	93%
Intensity Ratio	0.057 $(=\eta_f)$	0.943 $(=\eta_s)$	0.03 $(=\xi_f)$	0.45 $(=\xi_s)$
	1.00 $(=\eta_f+\eta_s)$		0.48*1) $(=\xi_f+\xi_s)$	
Microscopic Λ $W_{0\text{-}2}$			$\Lambda_{fast} = 0.53$ *2) $W_{0\text{-}2}^{dis} = 0.53 W_{0\text{-}1}$	$\Lambda_{slow} = 0.48$*3) $W_{0\text{-}2}^{hs} = 0.48 W_{0\text{-}1}$

*1) corresponding to the apparent asymmetric ratio Λ of 0.48 obtained from the luminescence spectrum in Figure 4-7.
*2) $\Lambda_{fast} = \xi_f / \eta_f$,
*3) $\Lambda_{slow} = \xi_s / \eta_s$

Table 4-5 Average lifetimes of Eu^{3+} ions $^5D_0 \rightarrow {}^7F_1$ and $^5D_0 \rightarrow {}^7F_2$ emission and fractional number located in higher symmetry sites in polytype GdF_3 nanocrystals.

	Average luminescence lifetime (ms)		Fraction of Eu^{3+} occupied in symmetric site
	$^5D_0 \rightarrow {}^7F_1$ (592 nm)	$^5D_0 \rightarrow {}^7F_2$ (619 nm)	
Hexagonal $GdF_3:Eu^{3+}$ (A)	11.8	7.5	71 %
Orthorhombic $GdF_3:Eu^{3+}$ (B)	6.7	4.8	69 %

As mentioned above, the $^5D_0 \rightarrow {}^7F_1$ emission peak at 592 nm from Eu^{3+} indicates a magnetic dipole transition in nature, which is insensitive to the atomic coordination around Eu^{3+} ions, however, the electric dipole transition of the $^5D_0 \rightarrow ^7F_2$ peak at 619 nm from Eu^{3+} is quite sensitive to the atomic coordination. Since the atomic coordination around Eu^{3+} ions or the site symmetry of Eu^{3+} ions is strongly dependent on the location of Eu^{3+} in the GdF_3 matrix, that is, interstitial, surface-state, or substitutional Eu^{3+} in GdF_3 nanocrystals, the decay behavior owing to electric-dipole and magnetic-dipole transitions includes information on the Eu location. The observed nonexponential decay curves (see Figure 4-13), expressed by Eq.(4-7), mean that at least two sites for Eu^{3+} ions exist in $GdF_3:Eu^{3+}$ nanocrystals for both hexagonal and orthorhombic structures. As mentioned in Chapter 2, luminescence with a short lifetime can be observed from Eu^{3+} ions positioned in very asymmetric sites (e.g., surface-state and interstitial sites), whereas luminescence with a long lifetime was observed from Eu^{3+} ions in a highly-symmetric site (substitutional site). Considering the crystal structures of GdF_3, the latter site is considered to be a crystallographic position in the substitution site of GdF_3 nanocrystals. As the decay lifetime of the $^5D_0 \rightarrow ^7F_2$ emissions fast component were estimated as 1.84 ms and 0.59 ms for hexagonal and orthorhombic crystals, respectively, it is longer than that in the case of $LaF_3:Eu^{3+}$ particles which are about 1.12 ms and 0.2 ms (See Chapter 3). By reference to the result of Chapter 3, the Eu fraction in high symmetric site as the function of reciprocal crystalline size (1/D) was shown in Figure 4-14. According to the TEM image of Figure 4-3, particle size was estimated about 80 nm for hexagonal $GdF_3:Eu^{3+}$ sample and the value 1/D was about 0.013 nm^{-1}, so it can be confirmed that Eu fraction located on the particle surface is very small. In Table 4-3 and Table 4-4, the asymmetric ratios for hexagonal $GdF_3:Eu^{3+}$ nanocrystals were estimated as A_{slow}=0.21 and A_{fast}=0.75, for orthorhombic $GdF_3:Eu^{3+}$ nanocrystals asymmetric ratio were estimated as A_{slow}=0.48 and A_{fast}=0.53, the A_{slow} values in both $GdF_3:Eu^{3+}$ polytype nanocrystals were according well with the data estimated in $LaF_3:Eu^{3+}$ nanocrystals (A_{slow}=0.25, see Chapter 2), it means that high symmetric site in both $GdF_3:Eu^{3+}$ polytype structures are substitutional site. On the other hand, the A_{fast} values in both $GdF_3:Eu^{3+}$ polytype nanocrystals are smaller than that in $LaF_3:Eu^{3+}$ nanocrystals (A_{fast}=12.0), so it can be confirmed that the disordered site in $GdF_3:Eu^{3+}$ polytype nanocrystals are different with that in $LaF_3:Eu^{3+}$ nanocrystals (surface-state site), it must be substitutional site with small displacement from the ideal position in polytype GdF_3 :Eu^{3+} lattice matrix. Since $\alpha\tau_f$ and $\beta\tau_s$ are strongly correlated with the number of Eu^{3+} ions in the above-mentioned sites, the fractional numbers of Eu^{3+} ions positioned in the substitution site of GdF_3 nanocrystals in both crystal systems can be estimated using the theory of transition probability and data obtained by decay curve analysis. The results are listed in Table 4-5. The fractional numbers were 71% for the hexagonal structure and 69% for the orthorhombic structure. This estimation is strongly supported by the fact that from the results of Rietveld refinement, most Eu^{3+} ions could substitutionally be positioned at the Gd^{3+} site in hexagonal and orthorhombic $GdF_3:Eu^{3+}$ nanocrystals. The similarity between the dispersibility of Eu^{3+} ions in the cores of hexagonal and orthorhombic $GdF_3:Eu^{3+}$ nanocrystals indicates that the stronger Eu^{3+} luminescence of hexagonal $GdF_3:Eu^{3+}$ nanocrystals is a consequence of the highly symmetric hexagonal structure and the shorter interatomic distance between Gd^{3+} and Eu^{3+} ions and, that the polytype structure is the main factor for determining the luminescence properties of these samples.

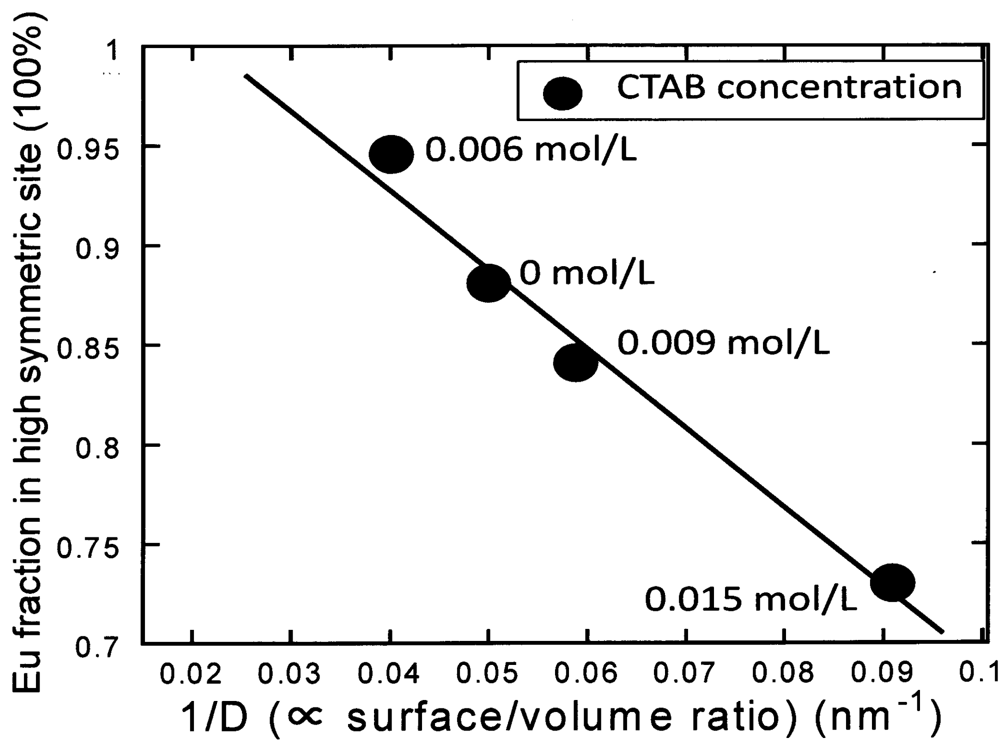

Figure 4-14 Eu fraction in high symmetric site as the function of reciprocal crystalline size (1/D), proportional to surface/volume ratio of $LaF_3:Eu^{3+}$ samples synthesized with different CTAB concentration.

4.4 Conclusion

In this Chapter, we succeeded in effectively characterizing hexagonal and orthorhombic $GdF_3:Eu^{3+}$ nanophosphors synthesized by the precipitation method. It was estimated by the Rietveld fitting of XRD patterns and by PL dynamics analysis that most of the doped Eu replaced Gd in both polytypes. In addition, Rietveld analysis indicated that the interatomic distance between Gd and substituted Eu in the hexagonal structure was shorter than that in the orthorhombic structure. A higher PL intensity owing to more efficient PL excitation via energy transfer from Gd^{3+} to Eu^{3+} in hexagonal $GdF_3:Eu^{3+}$ nanophosphors was demonstrated. This was explained by the energy transfer probability, taking account of the interatomic distance. The polytype control (hexagonal to orthorhombic) of matrix LnF_3 enabled us to enhance the energy transfer probability from Gd^{3+} to Eu^{3+} by varying the interatomic distance.

4.5 References

1. X.T. Zhang, T. Hayakawa, M. Nogami and Y, Ishikawa, "Selective synthesis and luminescence properties of nanocrystalline $GdF_3:Eu^{3+}$ with orthorhombic and hexagonal structures", J. nanomaterials, 2010, in press.

2. X.T. Zhang, T. Hayakawa, M. Nogami and Y, Ishikawa, "Variation in Eu^{3+} luminescence properties of $GdF_3:Eu^{3+}$ nanophosphors depending on matrix GdF_3 polytype", J. Alloys Compd. 2010, in press.

3. B.M. Tissue, "Synthesis and luminescence of lanthanide ions in nanoscale insulating hosts" Chem. Mater. **1998**, 10, 2837–2845.

4. Z.G. Chen, H.L. Chen, H. Hu, M.X. Yu, F.Y. Li, Q. Zhang, Z.G. Zhou, T. Yi, C.H. Huang, "Versatile synthesis strategy for carboxylic acid-functionalized upconverting nanophosphors as biological labels" J. Am. Chem. Soc. **2008,** 130, 3023–3029.

5. D.K. Chatteriee, A.J. Rufalhah, Y. Zhang. "Upconversion fluorescence imaging of cells and small animals using lanthanide doped nanocrystals" Biomat, **2008**, 29, 937–943.

6. P.R. Diamente, M. Raudsepp, F.C.J.M. van Veggel, "Dispersible Tm^{3+}-doped nanoparticles that exhibit strong 1.47 μm photoluminescence" .Adv. Funct. Mater. **2007**, 17, 363–368.

7. S. Sivakumar, P.R. Diamente, F.C.J.M, van Veggel, "Silica-coated $Ln3^{+}$-doped LaF_3 nanoparticles as new robust down- and up-converting biolabels", Chem.Eur. J. **2006**, 12, 5878–5884.

8. Z.J. Wang, F. Tao, L.Z. Yao, W.L. Cai, X.G. Li, "Controlled-synthesis and up-conversion luminescence of NaY F_4 : Yb, Er phosphors", Solid state communications, **2007**, 144, 255-258.

9. Z.L. Wang, J.H. Hao, Helen L. W. Chan. **"**Down- and up-conversion photoluminescence, cathodoluminescence and paramagnetic properties of $NaGdF_4 : Yb^{3+},Er^{3+}$ submicron disks assembled from primary nanocrystals**"**, J. Mater. Chem. **2010**, 20, 3178–3185.

10. X.Q. Zhang, X.P. Fan, X.S. Qiao, Q. Luo, "$NaGdF_4:Ce^{3+}$ and $(Ce,Gd)F_3$ nanoparticles: hydrothermal synthesis and luminescence properties", Materials Chemistry and Physics, **2010**, 121, 274–279.

11. M. Li, Z.-H. Hao, X.N. Peng, J.B. Li, X.F. Yu, and Q.Q. Wang, "Controllable energy transfer in fluorescence upconversion of NdF_3 and $NaNdF_4$ nanocrystals" Opt. Express, **2010**, 18, 3364-3369.

12. A. Mech, M. Karbowiak, L. Kepinski, A. Bednarkiewicz, W. Strek. "Structural and luminescent properties of nano-sized $NaGdF_4$: Eu^{3+} synthesised by wet-chemistry route" J. Alloys Compd, **2004**, 380, 315–320.

13. Allan Zalkin, D. H. templeton, "The crystal structures of YF_3 and related compounds" J. Am. Chem. Soc, **1953,** 75, 2453–2458.

14. R.E. Thoma, G.D. Brunton, "Equilibrium dimor- phism of the lanthanide trifluorides" Inorg. Chem, **1966,** *5*, 1937–1939.

15. K. Rotereau, Ph. Daniel, A. Desert, J.Y. Gesland, "The high-temperature phase transition in samarium fluoride, SmF.3 : structural and vibrational investigation", J. Phys. Condens. Matter **1998,** 10, 1431-1446.

16. S.V. Stankus, R.A. Khairulin, K.M. Lyapunov. "Phase transitions and thermal properties of gadolinium trifluoride", J.Alloys and Compounds, **1999**, 290, 30-33.

17. C.H. Dong, M. Raudsepp, Frank C. J. M. van Veggel, "Kinetically-determined crystal structures of undoped and La^{3+}-doped LnF_3" J. Phys. Chem. C, **2009**, 113, 472-478.

18. M. Wang, Q. L. Huang, J. M. Hong, X.T. Chen, Z.L. Xue, "Selective Synthesis and Characterization of Nanocrystalline EuF_3 with Orthorhombic and Hexagonal Structures", Cryst. Grow. Des. **2006,** 6, 1972-1974.

19. S.V. Stankus, R.A. Khairulin, K.M. Lyapunov, "Phase transitions and thermal properties of gadolinium trifluoride", J. Alloys Comp. **1999,** 290, 30-33.

20. D. Q. Chen, Y. S. Wang, Y. L. Yu, and P. Huang, "Structure and optical spectroscopy of Eu-doped glass ceramics containing GdF_3 nanocrystals", J. Phys. Chem. **2008**, C 112, 18943-18947.

21. S. Fujihara, S. Koji, T. Kimura, "Structure and optical properties of $(Gd,Eu)F_3$ nanocrystallized sol-gel silica films", J. Mater. Chem. **2004**, 14, 1331-1335.

22. L. Zhu, Q. Li, X. Liu, J. Li, Y. Zhang, J. Meng, X. Cao, "Morphological control and luminescent properties of CeF_3 nanocrystals", J. Phys. Chem. **2007,** C. 111, 5898-5903.

23. W. J. Crooks III,W. D. Rhodes, "Use of modeling for the prevention of solids formation during canyon processing of legacy nuclear materials", 2003 Westinghouse Savannah River Company Aiken, SC 29808,WSRC-TR-2002–00462.

24. Z. J. Miao, Z. M. Liu, K. L. Ding, B. X. Han, S. D. Miao, G. M. An, "Controlled fabrication of rare earth fluoride superstructures via a simple template-free route", Nanotechnology, **2007**, 18, 125605-125609.

25. L. Zhu, J. Meng, X. Q. Cao, "Facile synthesis and photoluminescence of the europium ion-doped LaF3 nanodisks", J. Inorg. Chem. **2007**, 24, 3863-3867.

26. M. Mansmann, "Die kristallstruktur von lanthantrifiuorid", Z. Kristaaogr. **1966**, 122, 375-398.

27. R.T. Wegh, H. Donker, K.D. Oskam, A. Meijerink, "Visible quantum cutting in $LiGdF_4$:Eu through down-conversion", Science (Washington, DC, U.S.) **1999**, 283, 663-666.

28. W. T. Carnall, P. R. Fields, K. Rajnak, "Electronic energy levels in the trivalent lanthanide aquo ions", J. Chem. Phys. **1968**, 49, 4424-4442.

29. F. Izumi, "The Rietveld Method,"ed. by R. A. Young, Oxford University Press, Chap. 13 (1993).

30. Handbook on the Physics and Chemistry of Rare Earths; Elsevier North-Holland: Amsterdam, The Netherlands, Vol. 5, 1982.

31. T. Förster, "Zwischenmolekulare energiewanderung und fluoreszenz" Ann. Physik. **1948**, 437, 55-75.

32. Joseph R. Lakowicz, "Principles of Fluorescence Spectroscopy", 2nd edition (1999)

Chapter 5. Summery

In this dissertation, size tuned $LaF_3:Eu^{3+}$ and polytype $GdF_3:Eu^{3+}$ nanoparticles were prepared. The effects of their crystal structure and particle size on Eu^{3+} luminescence properties were discussed. By analyzing Eu^{3+} ions position in host particles, luminescence properties in relation to the particles size and polytype structure were also discussed. The results of each chapter are summarized as follows.

In Chapter 2, the new method for estimating doped Eu^{3+} ions position in host particles were introduced. This method was based on Eu^{3+} ions typical luminescence properties. By analyzing Eu^{3+} ions $^5D_0 - {}^7F_{1,2}$ decay curves with double exponential function, Eu fractions located in each symmetric and distorted site in host particles can be estimated. This method as well as Rietveld refinement method should be the usefully tools in luminescence nanomaterials studies.

In Chapter 3 size tuned $LaF_3:Eu^{3+}$ nanocrystals were prepared via a hydrothermal route. A cationic surfactant CTAB was used to control particle size, particle growth mechanism was also discussed. The influences of post-annealing temperature and CTAB concentration on the size and morphology as well as on the photoluminescence (PL) properties were studied. It was found that the sample synthesized with 0.006 mol% CTAB and heated at 600°C with large particle size exhibited stronger luminescence intensity than others. By estimating Eu fraction in high symmetric site using the method introduced in Chapter 2, it was found that the most of Eu^{3+} ions (94.6%) were successfully incorporated in a higher symmetric site, in a LaF_3 lattice structure and as a result engaged in the strong PL. XRD patterns refinement analysis also showed the same result. The fraction of Eu ions located in a high symmetric site in LaF_3 lattice matrix was increased as particle size increased. Thus large particles induce strong luminescence.

Chapter 4 illustrated the correlation between host structure and doped Eu ions luminescence properties in polytype GdF_3. Hexagonal and orthorhombic $GdF_3:Eu^{3+}$ nanophosphors were separately synthesized via a simple soft chemical route at room temperature. The structure and morphology of $GdF_3:Eu^{3+}$ nanophosphors were controlled by using different fluoride precursors. Hexagonal $GdF_3:Eu^{3+}$

nanocrystals were formed when $NaBF_4$ was used as a fluoride precursor, while orthorhombic $GdF_3:Eu^{3+}$ nanocrystals were obtained with NaF or NH_4F fluoride precursor. Hexagonal $GdF_3:Eu^{3+}$ nanophosphors intrinsically exhibited stronger Eu^{3+} luminescence intensity under ultraviolet excitation. The Rietveld fitting of well-defined XRD data elucidated that the inter-atomic distances between Gd^{3+} ions in the hexagonal structure were shorter than those in the orthorhombic structure and that most Eu ions in $GdF_3:Eu^{3+}$ occupied Gd sites. The stronger luminescence in the hexagonal structure was conclusively explained by the much more efficient energy transfer from Gd to Eu in the hexagonal structure than in the orthorhombic structure, as determined on the basis of the inter-atomic distance between Gd and Eu.

In this thesis, the analysis of the correlationship between particle size and RE luminescence properties indicated that doping of Eu ions in large particles (in nano-size range) provide strong luminescence intensity, because the high fraction Eu ions posited substitution site in LnF_3 host lattice matrix and defect density is low in large particle according to the low surface/volume ratio. The correlationship studies between host structure and RE luminescence properties show that short distance between donor and accepter in LnF_3 hexagonal structure host induced high energy transfer probability and strong luminescence intensity.

For further future research work in LnF_3:RE photoluminescence material field, the study suggested that LnF_3:RE luminescence materials can be improved by choosing the host which is in large particles and easy for RE ions to be doped in and located in substitution site so as to minimize luminescence quenching, in the host there should be an acceptor matching with the RE donor and the distance between them must short so as to maximize the energy transfer probability.

Publications Including Studies in this Dissertation

1. Photoluminescence Properties and $^5D_0$ Decay Analysis of $LaF_3:Eu^{3+}$ Nanocrystals Prepared by Using Surfactant Assist

   Xiaoting Zhang, Tomokatsu Hayakawa and Masayuki Nogami,

   International Journal of Applied Ceramic Technology (in press) no. doi: 10.1111/j.1744-7402.2009.02433.x

2. Synthesis and luminescence properties of well-dispersed $LaF_3:Eu^{3+}$ nanocrystals.

   Xiaoting Zhang, Tomokatsu Hayakawa, Masayuki Nogami, Yukari Ishikawa

   Journal of Ceramic Processing Research (in press)

3. Selective Synthesis and Luminescence Properties of Nanocrystalline $GdF_3:Eu^{3+}$ with Hexagonal and Orthorhombic Structures

   Xiaoting Zhang, Tomokatsu Hayakawa, Masayuki Nogami, Yukari Ishikawa

   Journal of Nanomaterials (in press) doi:10.1155/2010/651326

4. Variation in Eu^{3+} Luminescence Properties of $GdF_3:Eu^{3+}$ Nanophosphors Depending on Matrix GdF_3 Polytype

   Xiaoting Zhang, Tomokatsu Hayakawa, Masayuki Nogami, Yukari Ishikawa

   Journal of Alloys and Compounds Volume 509, issue 5, February 2011, 2076-2080

5. Size-Dependence of $LaF_3:Eu^{3+}$ Nanocrystals on Eu^{3+} Photoluminescence Intensity

   Xiaoting Zhang, Tomokatsu Hayakawa and Masayuki Nogami

   IOP Conf. Series: Materials Science and Engineering **1** (2009) 012021

Other Publications

1. Blue light emission from Eu^{2+} ions in sol–gel-derived Al_2O_3–SiO_2 glasses

   Yukari Kishimoto, Xiaoting Zhang, Tomokatsu Hayakawa and Masayuki Nogami

   Journal of Luminescence Volume 129, Issue 9, September 2009, 1055-1059

2. Optical detection of near infrared femtosecond laser-heating of Er^{3+} doped Zn-Nb_2O_5-TeO_2 glass by green up-conversion fluorescence of Er^{3+} ions.

   M.Hayakawa, T.Hayakawa, X.T.Zhang, M.Nogami,

   Journal of Luminescence 2010, (in press) doi:10.1016/j.jlumin.2010.11.023

Acknowledgments

Firstly, I would like to thank my principal advisor, Assoc. Prof. Yukari Ishikawa. I really appreciate from my heart that she gave me all kinds of support for my PH. D. study. I also appreciate that she taught me things not only on research and work but also on interpersonal communication, during the two years, I definitely learned a lot from her. Without her, I could not achieve so much today.

Secondly, I would like to express my sincere gratitude to Prof. Fukuda Koichiro for his guidance throughout my doctoral studies, especially on crystal structure analysis with that the effect of crystal structure on LnF_3:RE luminescence properties were development in this studies. I would also like to thank to Assoc. Prof. Tomokatsu Hayakawa who led me into luminescence research field. For so many years, his numerous helpful discussions and kind advice always affected me on my study.

Thirdly, I want to say "thank you" to Prof. Masayuki Nogami for his endless support, his patience, and his acceptance of me as an overseas student studying under his guidance for master course.

I am very thankful to assoc. Prof. Masanobu Nakayama he taught me the technique of RIETAN software but also gave me much knowledge on crystallography for my research.

In addition, I would like to give my thanks to all members of Prof. Nogami, Prof. Kasuga, Fukuda, Hayakawa and Nakayama lab. for their participation in constructing fruitful discussion and meeting, and a friendly atmosphere. Here, I also want to extend my appreciation to the JFCC (Japan Fine Ceramics Center) members of Mrs Yabuda, Mrs Yamagishi, Mrs Suzuki, Dr. Yao, Mr. Sato, Mr. Matsumura and every one in JFCC for device testing, everyday interactions, and friendship.

Finally, I would like to show my parents and family members my sincere appreciation. Due to their comprehensive supports from mental to financial matters, I could continue my Ph. D. study without big trouble.

2011, January, Xiaoting Zhang